Kinetics of oil generation from brackish-lacustrine source rocks in the southern Bohai Sea, East China

Haoran Liang[a,b], Fanghao Xu[a,*], Kliti Grice[b], Guosheng Xu[a], Alex Holman[b], Peter Hopper[b], Deliang Fu[c], Qing Yu[a], Jiaju Liang[a], Deying Wang[d]

[a] *State Key Laboratory of Oil and Gas Reservoir Geology and Exploitation, Chengdu University of Technology, Chengdu 610059, China*

[b] *Western Australia Organic and Isotope Geochemistry Centre, The Institute for Geoscience Research, School of Earth and Planetary Sciences, Curtin University, GPO Box U1987, Perth, WA 6845, Australia*

[c] *Key Laboratory of Coal Exploration and Comprehensive Utilization, Ministry of Land and Resources, Xi'an 710000, China*

[d] *Bohai Oilfield Research Institute, Tianjin Branch, CNOOC, Tianjin 300459, China*

* Corresponding author: Fanghao Xu (Email: xufanghao17@cdut.edu.cn)

ABSTRACT

Oil generation (C_{14+} hydrocarbons) of three Type II kerogen samples isolated from brackish-lacustrine mudstones from Palaeogene strata (Ed_3, Es_1, Es_3) in the southern Bohai Sea was simulated by closed-system gold tube experiments. In addition, a series of complementary analyses (Rock-Eval pyrolysis, total organic carbon, vitrinite reflectance, trace element, X-ray diffraction and flash pyrolysis-gas chromatography–mass spectrometry) were also performed to identify the bulk geochemistry, palaeo-environment and chemical composition of the kerogen. The aim of this study was to achieve a better understanding of the kinetics of oil generation from lacustrine source rocks in the southern Bohai Sea. The results show that the three samples are Type II source rocks deposited in similar palaeo-environments (hot and arid climates, anoxic conditions, and brackish water in shallow to semi-deep lakes) with consequent similarity in the chemical compositions of their kerogens. The organic matter inputs are predominantly composed of lacustrine microalgae, with a relatively small contribution from land plants. The activation energies of oil generation from these samples show a range of 44–52 kcal/mol, with a frequency factor varying from 1.116×10^{14} to 1.274×10^{14} s^{-1}. Due to the similar palaeo-environments and chemical composition, samples in this study exhibit strong consistencies in kinetic parameters. Transformation ratio (TR) evolution curves of oil generation from the three samples, calculated under a linear heating rate (3 K/Ma), exhibit a slight difference, which varies within 4 °C at a given TR. Due to the great similarities of the three kinetic models, an average kinetic model for the Type II brackish-lacustrine source rocks in the southern Bohai Sea was established. This model integrates the characteristics of the three kinetic models and is still dominated by activation energy of 52 kcal/mol. The geological

temperature of the oil generation phase for the average model in the southern Bohai Sea is from 92–137 °C.

Keywords: Kinetics of oil generation; Type II kerogen; Palaeo-environment; Kerogen composition; Brackish-lacustrine source rock; Southern Bohai Sea

1. Introduction

Kerogen, a geopolymer of high molecular weight, is defined as the organic matter in sedimentary rocks that is not soluble in aqueous alkaline solvents nor common organic solvents (Tissot and Welte, 1984). Selective preservation and chemical condensation are the main pathways for the formation of kerogens (Larter and Horsfield, 1993). As burial depth increases, macromolecular matter in kerogen undergoes thermal breakdown, which results in petroleum (oil and gas) generation (Behar et al., 1997a).

Kerogen kinetics are not only used to obtain a better understanding of the thermal evolution of source rocks, but are also essential for basin modelling (Chen and Jiang, 2015). Four kinetic models have been reported to describe the progress of petroleum generation: (1) overall reaction model (a model with just one simple reaction) (Allred, 1966), (2) Friedman-type model (kinetic parameters in this model change along with the reaction process) (Friedman, 1964), (3) consecutive reaction model (final products are assumed to form through several continuous reactions) (Behar et al., 1997b, 2003, 2010), and (4) parallel reaction model (petroleum generation can be described by a series of parallel reactions) (Tissot et al., 1987; Ungerer et al., 1990; Burnham et al., 1995). It has been widely accepted that chemical reactions during petroleum generation can be described by first-order Arrhenius

reactions (Burnham et al., 1987; Sweeney and Burnham, 1990). The parallel reaction model with a single frequency factor and a discrete distribution of activation energies has been extensively used in many cases (Braun and Burnham, 1987; Burnham et al., 1989; Tegelaar and Noble, 1994; Dieckmann, 1998; Schenk and Dieckmann, 2004; Li and He, 2014; Abbassi et al., 2016). Due to the complexity of petroleum generation, only approximate kinetic results can be obtained when simulating the transformation of kerogen (Wood, 2018). Nevertheless, the Arrhenius equation still currently provides the best approximation to the key first-order reactions (Wood, 2018).

Pyrolysis experiments on immature kerogens in controlled conditions (relatively high temperatures and short durations) provide reliable data for the accurate calibration of kinetic parameters (Dieckmann, 2005). In turn, these kinetic parameters derived from laboratory experiments can be extrapolated to geological conditions to determine the progress of petroleum generation (Lewan et al., 1985, 2006; Schaefer et al., 1990; Dieckmann, 1998; Dieckmann et al., 2004; Peters et al., 2018). Closed system pyrolysis has been widely employed in the artificial petroleum generation from source rocks (Lewan et al., 1985, 2006; Landais et al., 1989; Dieckmann et al., 1998, 2000, 2004; Behar et al., 2010). Gold-tube pyrolysis is one of the most commonly used methods in confined system (Behar et al., 1997b; Fusetti et al., 2010b, 2010a; Lu et al., 2010; Mao et al., 2012; J. Wang et al., 2017; Huang et al., 2018). Monthioux et al. (1985, 1986) first conducted pyrolysis experiments on coal samples by using gold-tube confined system pyrolysis and proved that these pyrolysates were quite similar to natural crude oils. Moreover, the generated pyrolysates (e.g., oil, gas, water, etc.) and kerogens were in close contact with each other in compressed gold capsules. This reaction medium in gold-tube pyrolysis was more comparable to source rocks in natural

systems where the retained hydrocarbons were under great pressure from the overlying rocks and mainly absorbed by kerogens in source rocks (Xiang et al., 2016; Huang et al., 2019).

Palaeogene lacustrine mudstone (shale) is the main source rock in faulted basins of East China (Zhu et al., 2005; Li, 2015). More than 2.5 billion tons of oil sourced from lacustrine mudstone have been found in the Bohai Sea (offshore area of the Bohai Bay Basin), East China (Hao et al., 2009). Previous cases in the Bohai Sea (BS) focused on the gross kinetics or kinetics of gas generation (Gao et al., 2004; Liu et al., 2009; Wang et al., 2014; J. Wang et al., 2017, 2018; Niu et al., 2018), but none of them have focussed on oil generation. Therefore, the kinetic study of oil generation appears to be particularly important in the Bohai Sea. The kinetics of oil generation (C_{6+}) from lacustrine source rocks determined by gold-tube pyrolysis have been reported in other regions (Guo et al., 2008; Xiang et al., 2016; Huang et al., 2019). While the C_{6+} fraction can be further divided into C_{6-14} and C_{14+} fractions which are described by different kinetic models (Dieckmann et al., 2000; Liu et al., 2016). Previous studies conducted by gold-tube pyrolysis have made some attempts on the kinetics of oil (C_{14+}) generation from lacustrine Type II source rocks (Guo et al., 2009; Wei et al., 2012; Yan et al., 2019). However, there exists various problems in these cases. Firstly, the Type II kerogens in the some cases (Guo et al., 2009; Wei et al., 2012; Yan et al., 2019) were actually in mature stage which means a proportion of hydrocarbon potential has been consumed and would lead to the relatively high Ea distribution (Peters et al., 2006). On the other hand, some key information (calculation of kinetics; settings of parameter; frequency factor) of kinetics in some cases was not provided (Wang et al., 2003), thus the results cannot be validated and serve as an reference for kinetic study. In the present study, the above problems (immature lacustrine sample, detailed procedure) have been considered, and a better kinetic work of oil

(C_{14+}) generation determined by gold-tube pyrolysis has been presented.

This paper, based on comprehensive experiments (Rock-Eval, total organic carbon, vitrinite reflectance, trace element, X-ray diffraction, flash pyrolysis-GC–MS and gold tube pyrolysis), aims to determine the liquid oil potential of lacustrine source rocks and the kinetics of oil (C_{14+}) generation in the southern BS. Inorganic approaches, including trace element analysis and X-ray diffraction (XRD), were also employed to identify the depositional conditions of the samples. Flash Py-GC–MS was used to reveal the chemical structure of kerogen. The determination of the palaeo-environment and chemical composition of kerogen is beneficial to obtain a better understanding of the kinetic processes. In the present study, we established a typical (average) kinetic model of the Type II brackish-lacustrine kerogen in the southern BS. The results not only provide reliable data and new information for kinetic studies in the southern BS, but also serve as a reference for kinetic studies of brackish-lacustrine source rocks in East China or other regions that share a similar depositional environment.

2. Geological settings

The Bohai Bay Basin, one of the most petroliferous lacustrine basins in East China, is a Mesozoic-Cenozoic intraplate rift basin (Chen et al., 2017). The Bohai Sea (BS) is defined as the current offshore area of the Bohai Bay Basin (Wang et al., 2014). As shown in Fig. 1, the study area is located in the southern BS and consists of two sags (Laizhouwan Sag, Huanghekou Sag) separated by four uplifts (Bonan low uplift, Laibei low uplift, Kendong uplift and Weibei uplift).

The southern BS experienced two periods of tectonic movement during the Cenozoic

Era, known as the syn-rift and post-rift periods (Fig. 2) (Hsiao et al., 2004). The tectonic evolution in the southern BS was determined by both normal faults and strike-slip faults (Liu et al., 2016; Zhang et al., 2017): Stage I and stage II of the syn-rift period were predominately controlled by subparallel EW-trending normal faults. Stage III of the syn-rift period was under the superimposition effect of the subparallel EW-trending normal faults and the NNE-trending strike-slip faults (Fig. 2).

The Palaeogene strata in the study area include the Palaeocene Kongdian (Ek) Formation, the Eocene Shahejie Formation (Es) and the Oligocene Dongying Formation (Ed) (Fig. 2). These formations were deposited in alluvial, fluvial, deltaic, salt lake or semi-deep to deep lake facies (Allen et al., 1997; Xin et al., 2013; Wen et al., 2014). The Shahejie Formation and Dongying Formation can be divided into four members and three members, respectively (Fig. 2). Several sets of source rocks (Es_4, Es_3, Es_{1-2}, and Ed_3) have been discovered as the main source rocks in the southern BS (L. Wang et al., 2011; Yang et al., 2011; Niu, 2012; Wu et al., 2015). The Neogene strata, mainly controlled by fluvial and shallow lake facies (Allen et al., 1997; L. Wang et al., 2011), are composed of the Guantao Formation (Ng) and Minghuazhen Formation (Nm). The Quaternary in the study area is dominated by marine sediments (Zhu et al., 2015).

3. **Materials and methods**

3.1. Sample description and preparation

In this study, three source rock samples were collected from Well HHK25-2-A and Well LZW10-3-A (Fig. 1b). The three grey mudstone samples correspond to the three main source rock layers in the southern BS (Table 1). All these samples were cleaned in an

ultrasonic bath with distilled water and sonicated several times to remove the drilling mud. Then these samples were dried up and cleaned several times by ultrasonic cleaner again with the mixture of dichloromethane and methanol (9:1, v/v) to exclude possible organic contamination from external (artificial) sources.

3.2. Total organic carbon, Rock-Eval pyrolysis and Vitrinite reflectance

Total organic carbon, Rock-Eval and vitrinite reflectance were tested to determine the basic geochemical characteristics of the source rock samples. Samples were crushed to 100 mesh by using an agate mortar and pestle. The detailed steps of total organic carbon analysis follows Wang and Guo (2019). Samples were digested with a HCl solution (5%) to eliminate the inorganic carbonate fraction. Then samples were cleaned using distilled water and dried in an oven at 50 °C. The total organic carbon (TOC) was measured with a Leco CS-230 Carbon/Sulfur Analyzer with an error no more than 0.5%. Both the original rock samples and kerogen samples were measured for TOC.

Rock-Eval measurements followed Lafargue et al. (1998) using a Rock-Eval 6 instrument. Free hydrocarbon (S_1), pyrolysis hydrocarbon (S_2), CO_2 yield (S_3) and the temperature of maximum pyrolysate (Tmax) were determined.

The detailed preparation and measurement of vitrinite reflectance (%Ro) can be found in Liang et al. (2019). Sample were crushed into particles (2–3 mm), mounted in liquid epoxy on glass slides, and then polished. The measurement of %Ro was performed on a Leco CTR6000M Photometry Microscope and at least 25 points were measured for each sample. The final vitrinite reflectance was the arithmetic mean value of these points.

180 *3.3. Trace element and mineralogy analysis*

181 The collected rock samples were ground using an agate mortar and pestle to 200 mesh.
182 Approximately 50 mg of each sample was weighed into Teflon beakers and digested in a
183 series of acid digestions using HNO_3 and HF until a clear solution was obtained, following
184 Wei et al. (2018). The solution was diluted 1:1000 by mass and analysed on a Finnigan MAT
185 inductively coupled plasma mass spectrometer (ICP-MS). Trace elements (V, Co, Ni, Cu, La,
186 Sr, and B) were measured with a relative standard deviation no more than 5%.

187 Measurements of mineral compositions by X-ray diffraction (XRD) have been
188 described in detail by Wang and Guo (2019b). The samples were ground to <40 μm with an
189 agate mortar and pestle. The powdered samples were scanned by an Ultima IV X-ray
190 diffractometer with Cu-Ka radiation. The generator settings were 40 kV and 30 mA. X'Pert
191 High Score software was used to identify the mineral type and content. Note that the clay
192 mineral content was measured for samples of <5 μm fractions.

193

194 *3.4. Inorganic proxies of palaeo-environment proxies*

195 Commonly used inorganic proxies were employed to identify the palaeo-environment
196 including the Sr/Cu ratio (Cao et al., 2015; Alexandrine et al., 2019). A high ratio denotes hot
197 and arid climatic conditions, while a low ratio indicates warm and humid conditions (Table 2).
198 In addition, a high V/V+Ni ratio is an effective proxy of reducing (anoxic) conditions, while a
199 low ratio reflects oxic to dysoxic conditions (Greenwood et al., 2013; Kayode et al., 2014).
200 Moreover, boron has been widely accepted as a quantitative proxy of palaeo-salinity, due to
201 the strong correlation between boron and salinity in modern aqueous systems (Adams et al.,
202 1963; Couch, 1971). In consideration of the different boron absorption capacities for each

type of clay mineral, palaeo-salinity can be calculated according to the following formulae (Couch, 1971):

$$B_k = B_{clay}/(4X_i + 2X_s + X_k) \quad (1)$$

$$\log B_k = 1.28\times\log (S_p) + 0.11 \quad (2)$$

Here, B_k refers to the abundance of boron absorbed in kaolinite (μg/g), B_{clay} is the boron content in the clay fraction, which excludes the impact of inherited (terrestrial) boron (μg/g), X_i, X_s and X_k represent the proportion of illite, smectite and kaolinite in the clay fraction (%), respectively, and S_p is the palaeo-salinity (in parts per thousand, ppt).

Cobalt (Co) can be used as a quantitative parameter for the palaeo-water depth (Zhou et al., 1997, 1999; Zhang et al., 2011). The abundance of Co in sedimentary rock is mainly controlled by the sediment source and cosmic dust, in which the sedimentary rate of Co is nearly constant (Wu and Zhou, 2000). Formulae were first proposed by Zhou et al. (1997):

$$SR_{Sample} = SR_{Lacustrine}\times Co_{Lacustrine}/(Co_{Sample} - \alpha\times Co_{Terrigenous}) \quad (3)$$

$$A = La_{Sample}/La_{Terrigenous} \quad (4)$$

$$D = 3.05\times10^5/SR_{Sample}^{1.5} \quad (5)$$

Where SR_{Sample} and $SR_{Lacustrine}$ represent the sedimentation rate of sample and normal lacustrine mudstone, respectively (mm/y); $SR_{Lacustrine}$ is always 0.15–0.30 mm/y in lacustrine mudstone (Zhang et al., 2011). $Co_{Lacustrine}$, Co_{Sample} and $Co_{Terrigenous}$ refer to the cobalt abundance in normal lacustrine mudstone (20 μg/g), samples and terrigenous clasts (4.68 μg/g), respectively (Zhang et al., 2011), α is the correction coefficient of the terrigenous cobalt, indicating the terrigenous contribution. La_{Sample} and $La_{Terrigenous}$ are the lanthanum abundance in samples and terrigenous clasts, respectively, where $La_{Terrigenous}$ is 39 μg/g (Zhang et al., 2011) , and D is the palaeo-water depth of the sample (m).

3.5. Chemical treatments of isolated kerogen

Rock samples were ground to powder (<100 mesh) and treated with HCl and HF to isolate the kerogens from the rocks following the steps proposed by Saxby (1970). All of the kerogen samples were extracted in a Soxhlet apparatus for 72 h to remove the soluble organic matter using a mixture of dichloromethane and methanol (9:1, v/v) for the preparation of flash pyrolysis-GC–MS and gold tube pyrolysis.

3.6. Flash pyrolysis-GC–MS

Kerogen samples (approximately 4 mg) were loaded into quartz pyrolysis tubes. Flash pyrolysis was performed using a CDS Analytical Pyroprobe 5250 equipped with an autosampler and connected to the GC inlet by a heated transfer line (300 °C). The kerogen samples were pyrolysed at 650 °C for 20 s. An Agilent 6890 gas chromatograph and an Agilent 5973 mass selective detector were used to analyse the pyrolysate. Helium gas was employed as the carrier for GC separation and pyrolysate transfer. The initial temperature of the GC oven was –20 °C (held for 1 min), which was achieved using liquid CO_2. The oven was heated to 40 °C at a rate of 8 °C/min, then heated to a final temperature 320 °C at a rate of 4 °C/min, and held at 320 °C for 25 min. The transfer line temperature was 320 °C. The full-scan mass spectrum from 15 to 600 Da was measured with an electron energy of 70 eV. A blank flash pyrolysis run, using an empty quartz tube, was carried out before the analysis of each sample to avoid contamination.

3.7. Closed system-gold tube pyrolysis

Gold tube pyrolysis was conducted in a confined and anhydrous system following the procedures described by Wei et al. (2012). Each kerogen sample was divided and loaded into 24 gold tubes (40 mm length, 0.2 mm wall thickness and 3 mm i.d.) that were welded on one end. The weight of sample loaded in each tube decreased from 100 mg to 10 mg with increasing target temperature. Argon was flushed into the tubes for 15 min to displace air, then the other end of the tube was sealed by arc welding.

The 24 tubes were divided into two groups of twelve. One group was heated at a rate of 2 °C/h, while the other was heated at 20 °C/h. The sealed tubes in each group were placed into separate autoclaves in the same oven, with each autoclave having a different maximum target temperature and containing one tube from each kerogen sample. The heating temperature was programmed to increase from the ambient temperature (25 °C) to 200 °C over 10 h and then increase to a maximum of 440 °C at a rate of 20 °C/h (or to 400 °C at 2 °C/h). Autoclaves were removed from the oven once the target temperature for that autoclave had been reached. For the 2 °C/h group the target temperatures ranged from 290 °C to 400 °C in 10 °C intervals, while for the 20 °C/h group the target temperatures ranged from 330 °C to 440 °C in 10 °C intervals.

The fan set at the bottom of the oven facilitated heat circulation and made the difference in temperatures between the 12 autoclaves no more than 1 °C. Note that the three gold tubes filled with the three samples from Es_3, $Es_{1\text{-}2}$, and Ed_3 were placed into each autoclave. This step ensured that the samples from different layers experienced the same degree of thermal simulation. Thus, experimental error between the samples could be minimised.

Pressure in the autoclave, controlled by a set of pressure devices, was maintained at 50 MPa with an error of < 1 MPa. Each autoclave was connected to a water pipe used to fill and drain water. Pressure in the autoclave was monitored by a pressure programme and adjusted by adding water from the pump or expelling water from the drain valve.

The autoclaves were removed from the oven at their target temperatures and quenched in a cold-water bath. Then, the gold tubes in the autoclave were removed and cut in half. The hydrocarbons in the gold tubes were extracted in a Soxhlet apparatus for 72 h with a mixture of DCM and methanol (9:1, v/v). A rotary evaporator was used to concentrate the extracts. Finally, the C_{14+} fraction (oil) was collected in bottles and weighed.

Moreover, it should be noted that the C_{14+} fraction measured is the mass of liquid hydrocarbons generated by the kerogen samples. The mass of C_{14+} fraction needs to be transformed to the oil yields of source rocks by the following equation (6):

$$\beta = M_{C14+}/(M_{sample} \times TOC_{kerogen}) \quad (6)$$

Where β is the oil yield from the OM (mg/g $_{TOC}$); M_{C14+} represents the mass of C_{14+} fraction generated by kerogen sample (mg); M_{sample} represents the mass of kerogen sample loaded into the tube (mg); $TOC_{kerogen}$ is the total organic carbon content of kerogen (wt%).

3.8. Kinetic analysis

The transformation ratio (TR), i.e. the ratio of kerogen already transformed to hydrocarbon (Tissot and Welte, 1984), is one of the most significant factors for kinetic calculation. TR can be calculated using equation (7).

$$TR = \beta/\beta_{maximum} \quad (7)$$

Where TR is the transformation ratio; β indicates the cumulative oil yield at a certain

pyrolysis temperature; $\beta_{maximum}$ represents the primary maximum cumulative oil yield.

Based on the pyrolysis data from the laboratory, the TR at each pyrolysis temperature can be obtained and used as the input data for calculation of the kinetics. Special kinetic software (Kinetic 2000 developed by Lawrence Livermore National Laboratory (LLNL) and Humble Instruments & Services), was employed to fit the kinetic parameters of oil generation, including frequency factors and activation energies.

The first-order reaction in parallel with a single frequency factor and a discrete distribution of activation energies was chosen as the preferred calculation method. As recommended by Burnham (2017), 1 kcal/mol was set as the spacing of discrete activation energies.

4. Results

4.1. Bulk geochemical characteristics

Rock-Eval, total organic carbon and vitrinite reflectance were performed to obtain the basic geochemical data of samples (Table 1). Vitrinite reflectance (%Ro) and Tmax showed relatively low values of 0.37–0.39% and 427–431 °C, respectively. These two parameters indicate the immaturity of these samples. Total organic carbon (TOC) content of the rock samples is 2.8–4.3%, and the hydrogen index (HI) was 559–613 mg/g. To avoid the uncertainty of kerogen type by only using HI, the analysed samples were projected onto pseudo-van Krevelen diagrams of HI–OI and HI–Tmax to identify the kerogen type objectively. As shown in Fig. 3, the samples in the present study exhibited the features of Type II kerogen.

317 *4.2. Palaeo-environmental proxies*

318 The trace element data of the rock samples are presented in Table 3. Several effective
319 trace element proxies found by previous researchers, i.e. V/(V+Ni), Sr/Cu, Co, and B were
320 employed to determine the palaeo-environment.

321 The concentrations of trace elements in the samples do not vary substantially. As
322 shown in Table 3, ratios of V/(V+Ni) in the samples show a narrow range of 0.70-0.73. The
323 Sr/Cu ratios of the samples are 17.1–20.8. In addition, the concentrations of Co are 14.4–16.0
324 μg/g. Based on equations 3–5, the palaeo-water depths of the samples of D3, S1, and S3 are
325 approximately 27, 30 and 38 m, respectively.

326 Clay mineral types and proportions, listed in Table 4, provide the foundation for
327 reconstructing the palaeo-salinity by using boron. The total clay content and clay mineral
328 contents (I', S', and K) of the three samples exhibit similar values (Table 4). The boron
329 concentrations in the samples ranged from 35.3 to 46.8 μg/g.

330 The inherited boron content can be estimated by the method proposed by Ye et al.
331 (2016): It is assumed that the lowest boron sample at the same K_2O content contains primarily
332 the inherited boron and only a very small amount of dissolved boron from lake water. The line
333 of best fit between the K_2O (representing the content of illite) and boron content of the lowest
334 boron samples always shows a strong correlation. The boron content on this line can be
335 assumed to be the inherited boron content when the K_2O content is zero. Abundant samples
336 with K_2O and boron contents in the Huanghekou Sag of the southern BS have been published
337 (Zhuang et al., 2010). Therefore, these data can be used to determine the inherited boron
338 content in the southern BS, which was estimated to be 18 μg/g by the method of Ye et al.
339 (2016).

340 The palaeo-salinity, calculated by equations (6) and (7), is in a narrow range of
341 5.0–7.4 ppt (Table 4). Sample S1 has the highest palaeo-salinity, while sample S3 has the
342 lowest palaeo-salinity.
343
344 *4.3. Pyrolysates from flash pyrolysis-GC–MS*
345 The total ion chromatograms (TICs) from flash pyrolysis-GC–MS of the
346 three-kerogen samples at 650 °C are presented in Fig. 4a–c. All the samples display dominant
347 homologous and bimodal distributions of *n*-alkane/*n*-alk-1-ene doublets from C_6 extending to
348 C_{29}, with the maxima at C_6 and C_{21}. The aliphatic hydrocarbons of the three samples show
349 identical minima at C_{14}. Monoaromatic compounds, such as benzene and short-chain
350 alkylated benzenes (e.g., toluene, ethylbenzene and m-xylene), make up the majority of
351 aromatics (Fig. 4d–f). Mass chromatography of *m*/*z* 217 identified C_{27}–C_{29} steranes, although
352 the exact species (e.g., C_{27} ααα20R, C_{27} αββ20S, C_{27} ααα20S, etc.) could not be determined
353 due to the low abundance of steranes. C_{27} steranes and C_{28} steranes account for the majority of
354 steranes in all these samples (Fig. 4g–i). A series of parameters for the analysis of pyrolysates,
355 following Zhang et al. (2014), were employed to reflect the composition of the pyrolysates
356 (Table 5). Values of parameter 1 and parameter 2 vary with narrow ranges of 0.65–0.68 and
357 0.32–0.35, respectively. Parameter 3, which represents the amount of aromatics (Zhang et al.,
358 2014), is between 2.30 and 2.72. Parameter 4 and 5, indicating the relative contents of toluene
359 and benzene in monoaromatics, are 0.42–0.47 and 0.10–0.24, respectively. The variation
360 pattern of parameter 4 is the same as for parameter 3. However, for parameter 5, S1 has the
361 highest value, whereas D3 exhibits the lowest value. Parameter 6, a maturity index (van Graas
362 et al., 1981), has the range of 0.34–0.47.

363

364 *4.4. Oil pyrolysates from gold tube pyrolysis*

365 The cumulative oil yields (C_{14+} fraction) from the gold tube pyrolysis experiments are
366 presented in Table 6 and Fig. 5. The cumulative oil yields under 2 °C/h are approximately
367 equal to (or slightly lower than) the yields under 20 °C/h. Moreover, the curve of the yields
368 under 2 °C/h and 20 °C/h exhibit similar variations (Fig. 5). Yields of all the samples first
369 increase to the maximum values and then decrease with increasing pyrolysis temperatures.
370 The decrease in oil yields is associated with secondary hydrocarbon cracking in the confined
371 system (Wei et al., 2012).

372 All three samples reached their maximum oil yields at 390 °C under 20 °C/h and
373 350 °C under 2 °C/h. As shown in Table 6, sample S3 has the highest maximum yield (523
374 mg/g TOC under 20 °C/h; 485 mg/g TOC under 2 °C/h) among all the samples, while D3
375 and S1 present very similar maximum yields under the different heating rates (447 and 441
376 mg/g TOC under 2 °C/h; 458 and 456 mg/g TOC under 20 °C/h).

377

378 *4.5. Determination of primary maximum oil yield*

379 The impact of secondary oil cracking is an inevitable problem during the highly
380 mature stage of source rocks. Based on the comparison of results from open and closed
381 system pyrolysis, Dieckmann et al. (1998, 2000) contended that the overlap between primary
382 oil generation and secondary oil cracking was quite narrow because the latter commenced
383 very soon after the former has come to an end. A recent study (Sun et al., 2015) determined by
384 gold-tube pyrolysis (using different heating methods) came to a similar conclusion. To reduce
385 the impact of secondary oil cracking we used Sun et al. (2015) as a guide to identify the

386 primary maximum oil yields in the present study. In this study oil yields of the two lacustrine
387 kerogen samples were measured by gold-tube pyrolysis using two heating methods: a
388 continuous heating method and step by step heating method. The former is the method we
389 employed in present study. For the latter, the sample is heated to different target temperatures
390 discontinuously. C_{14+} generated is extracted from the sample when the first target temperature
391 is reached. Then the extracted sample was re-loaded into the gold tube and heated to its next
392 target temperature. This operation is repeated until the last target temperature. In this way, the
393 oil generated at different stages can be well preserved and measured. In addition, the impact
394 of secondary cracking to oil yields in gold tube pyrolysis can be reduced.
395 The oil generation of kerogens in study of Sun et al. (2015) was from 300 °C to
396 380 °C. The two heating methods exhibited nearly the same oil yields when pyrolysis
397 temperature was 300–360 °C. The secondary cracking gradually occurred at the end of oil
398 generation when temperature was above 360 °C, consistent with the ideas of Dieckmann et al.
399 (1998, 2000). The maximum oil yields of the two lacustrine kerogen samples using the
400 continuous method were 90% of that in “step by step” method. Moreover, the temperature gap
401 of the maximum yield from the two method was 10 °C.
402 The gold tube pyrolysis in present study and in the case of Sun et al. (2015) were
403 performed on the same instrument and the samples are all lacustrine kerogens. If the “step by
404 step” method is treated as the method closest to geological conditions, then the findings of
405 Sun et al. (2015) can be used to calibrate the maximum oil yield in a continuous system. In
406 this way, the primary maximum oil yields (primary maximum yield = maximum $yield_{continuous}$
407 $_{method}$/90%) and corresponding temperatures of samples can be estimated for the present work
408 (Fig. 5). The primary maximum oil yields for sample D3, S1 and S3 are 497, 490 and 539

mg/g TOC, respectively.

4.6. Kinetic results

Kinetic analyses of oil generation, in terms of the frequency factor (A) and activation energy (Ea) distribution were calculated based on the closed-system pyrolysis data. Detailed information on the derived parameters is listed in Table 7. The discrete distributions of Ea are given by bar graphs (Fig. 6d–f). Type II kerogen samples in this study are characterized by a relatively broad distribution of Ea (44–52 kcal/mol) rather than a narrow range of Ea. The lines of best fit and experimental transformation ratio (TR) data are shown in Fig. 6a–c.

For the generation of the C_{14+} fraction, the samples in this study exhibit similar kinetic features (Ea range, A and predominant Ea): Oil generation from samples D3, S1 and S3 requires an Ea range of 46–52 kcal/mol, 46–52 kcal/mol, and 44–52 kcal/mol and A values of 1.121×10^{14} s^{-1}, 1.116×10^{14} s^{-1}, 1.274×10^{14} s^{-1}, respectively (Table 7). Samples D3, S1 and S3 show similar average Ea value of 49.9, 50.0 and 50.2 kcal/mol, respectively (Table 7).

5. Discussion

5.1. Determination of palaeo-environment

The depositional environment is an important influence on the composition, preservation and quality of OM (Tribovillard et al., 2006; Harris et al., 2013). However, the palaeo-environments of source rock samples have not been considered in previous kinetic studies, and the palaeo-environment of the Palaeogene in the southern BS has rarely been

studied. The concentrations and ratios of trace elements are important proxies to reconstruct the palaeo-depositional conditions of marine and lacustrine systems (Jones and Manning, 1994; Tribovillard et al., 2006; Harris et al., 2013), and so several were employed to achieve a better understanding of the depositional conditions in the BS.

Palaeo-salinities of the samples are estimated to be 5.0–7.1 ppt, suggesting brackish water (mesohaline) in the palaeo-lake (Table 2). The Sr/Cu ratio has a positive correlation with the degree of drought, so the high ratios of Sr/Cu (17.1–23.3) from different layers in the southern BS were formed under a hot and arid climate (Table 2). The palaeo-water depths of the samples (ca. 27–38 m) indicate environments of shallow to semi-deep lakes (Table 2). Such sedimentary environments are considered to be suitable for producing high-quality source rocks in the Bohai Bay Basin (Niu, 2012; Wu et al., 2015). The depositional environment of sample S3 and S1 is a semi-deep lake. The palaeo-water depths of samples D3 is close to the lower limit (30 m) of semi-deep lakes (Table 3). The V/(V+Ni) ratios (0.65–0.73) suggest the presence of anoxic conditions, which is beneficial for the preservation of organic matter (Tribovillard et al., 2006).

In summary, it was found that the three Type II samples in this study were deposited in similar sedimentary environments (hot and arid climate, anoxic conditions, and brackish water in shallow to semi-deep lakes). This finding implies that the samples in this study may share similar kerogen compositions and kinetic characteristics.

5.2. Kerogen composition from pyrolysis-GC–MS

Flash pyrolysis is considered to be one of the most efficient tools for probing the chemical structures of kerogens (Gelin et al., 1995). It has been demonstrated that lacustrine

455 kerogens exhibit bimodal distributions of pyrolysates and abundant C_{20+} proportions (Derenne
456 et al., 1994; Grice et al., 2003), while marine kerogens can produce a unimodal distribution
457 with a maximum around *n*-C_{13} and relatively low abundance of C_{20+} (Horsfield, 1989;
458 Flaviano et al., 1994). As shown in Fig. 4a–c, the pyrolysate distributions exhibit typical
459 characteristics of lacustrine kerogens. Parameters of the three samples exhibit similar values
460 with only slight differences (Table 5), indicating their similar chemical structures. Pyrolysates
461 of these samples are all dominated by short to middle chain aliphatics and monoaromatics
462 (Fig. 4a–f).

463 The pyrolysate distributions were compared with a previous study of Zhang et al.
464 (2014) in which both lacustrine Type I and II kerogens from NE China were analyzed by flash
465 pyrolysis-GC–MS. The two types of kerogens were distinguished by different pyrolysate
466 distributions and compositions. The pyrolysates (aliphatic distribution, long-chain aliphatics,
467 aromatic compounds and abundance, etc.) of samples in the present study are quite different
468 from lacustrine Type I kerogens, but very close to the Type II kerogens of Zhang et al. (2014).
469 This evidence further supports our previous analysis of kerogen type from bulk geochemical
470 experiments (e.g., Rock-Eval Pyrolysis).

471 *n*-Alkane/*n*-alk-1-ene doublets dominate the pyrolysates of the kerogen samples and
472 reveal the abundant presence of aliphatic macromolecular constituents (Fig. 4d–f). These are
473 typical of pyrolysates of algaenan biopolymers, which are found in the cell walls of specific
474 lacustrine microalgae (Largeau et al., 1986; Sinninghe Damsté et al., 1993; Gelin et al., 1994,
475 1995, 2003a; Audino et al., 2002; Holman and Grice, 2018).

476 Plant-derived components always produce high proportions of aromatics, especially
477 complex aromatics (PAHs) (Solli and Leplat, 1986; Yoshioka and Takeda, 2004). The PAHs in

478 the present study, such as methylnaphthalenes, ethylnaphthalenes and dimethylnaphthalenes,
479 were detected but in low abundance (Fig. 4d–f), while the majority of aromatic compounds
480 are monoaromatic, indicating a relatively low contribution from land plants.
481 The distribution of steranes provides valuable information on organic matter inputs
482 (Huang and Meinschein, 1979; Volkman, 1988). C_{27} sterols (steranes) are mainly from algae,
483 while C_{29} sterols (steranes) are more typically associated with land plants although microalgal
484 sources are known (Volkman, 1986; He et al., 2018). Compared to C_{27} and C_{28} steranes, an
485 increased abundance of C_{29} steranes suggests a greater contribution of land plants to the OM
486 (Grice and Eiserbeck, 2013). However, it is difficult to assign any sterane to a specific group
487 of organisms (Kodner et al., 2008). For example, green algae can be the possible potential
488 source of C_{29} steranes (Volkman, 1988; Volkman et al., 1994). In addition, the specific sources
489 of C_{28} steranes remains uncertain. Fungi and microalgae such as diatoms may be the possible
490 source of C_{28} steranes (Volkman, 1986; Grice and Eiserbeck, 2013; He et al., 2018). As shown
491 in Fig. 4g–i, C_{27} steranes and C_{28} steranes account for the majority of steranes in all these
492 samples, suggesting high inputs of lacustrine (planktonic) microalgae, while the relatively low
493 proportion of C_{29} steranes is consistent with the low amounts of PAHs, indicating the low
494 inputs of land plants.
495 Prist-1-enes, which are usually attributed to the phytyl side chain of chlorophyll
496 (Larter et al., 1979; Höld et al., 2001), were observed in these samples (Fig. 4a–c). Parameter
497 6, varying from 0.34 to 0.47, suggests that the samples are of low maturity (Zhang et al., 2014)
498 which is consistent with vitrinite reflectance and Tmax data in Table 1.
499 Overall, flash pyrolysis provides more evidence for the kerogen type of our samples
500 indicating their similar chemical structure (Type II_1 kerogen). OM inputs of samples are

mainly sourced from the algaenans of lacustrine microalgae. Land plant input makes up a small proportion of the total OM.

5.3. Kinetics of Type II kerogen

The parallel reaction model with a single A and a discrete distribution of Ea was used to calculate the kinetic parameters in this study. The curves of the TR derived from the kinetic parameters show good agreements with the experimental data (Fig. 6a–c), indicating that the kinetics fitting results are credible (Tegelaar and Noble, 1994). In consideration of the linear correlation between Ea and A in logarithm form (Wood, 2018), we focus on the discussion and comparison of Ea.

As shown in Table 4, the kinetic parameters of the three samples in the present study share the same predominant Ea (52 kcal/mol), similar average Ea values (49.9–50.2 kcal/mol) and Ea ranges (44–52 kcal/mol). Only slight differences can be observed in these samples. Kinetic parameters describe the molecular structure of kerogen under thermal stress (Tegelaar and Noble, 1994). The thermal stability of kerogen is determined by the dissociation energies of different chemical bonds, such as various carbon and heteroatomic bonds (Wei et al., 2012). The consistencies of kinetic parameters between samples can be attributed to the close similarities in kerogen chemical structure and the formation environment of the samples. Moreover, the Ea distributions of the samples are more concentrated in high Ea (52 kcal/mol), while distributions of relatively low Ea parts (44–51 kcal/mol) are relatively dispersed. It has been recognized that long-chain aliphatics have lower bond dissociation energy than that of short- to middle-chain aliphatics (Jiang et al., 2008), resulting in the increased proportions of low Ea in samples having abundant

long-chain aliphatics. Hence, the predominant Ea (52 kcal/mol) in the present study may be associated with the high proportion of short- to middle-chain aliphatics, while the relatively low Ea may be associated with the long-chain aliphatics which are in relatively low proportion (Table 5).

The kinetic behaviour of kerogen is influenced by a variety of factors (Wood, 2018), but kerogen type is the one most commonly discussed (Hunt et al., 1991; Tegelaar and Noble, 1994; Reynolds et al., 1995; Lewan et al., 2006; Peters et al., 2018). Although the exact Ea values for different types of kerogen remains controversial (Zhang et al., 1983; Pei and Zhou, 1989; Jiang et al., 2008; Liu et al., 2009; Chen and Jiang, 2015), researchers have reached a consensus on the Ea distribution (Tissot and Welte, 1984; Klomp and Wright, 1990; Behar et al., 1997b): Type I kerogen has a quite narrow Ea distribution, while Type III kerogen exhibits a very broad range and Type II kerogen displays an intermediate range. Samples in the present study share similar Ea results and exhibit a range of 44–52 kcal/mol, suggesting the typical intermediate Ea range of Type II kerogen. This further validates the previous evidence on kerogen type. Moreover, the average Ea values of oil (C_{14+}) generation in the present study are relatively low (49.9–50.2) compared with that (51 kcal/mol) of oil (C_{6+}) generation in Type II kerogen (Guo et al., 2008). This can be attributed to the different generation mechanisms that the generation of C_{6-14} fraction significantly lags behind that of C_{14+} fraction, which results in the relatively low Ea of the C_{14+} fraction (Dieckmann et al., 2000; Liu et al., 2016).

Apart from kerogen type, organic sulfur may play an important role in the kinetics of petroleum generation (Lewan, 1998): Sulfur-rich samples are characterised by low Ea because the S–S and C–S bonds are more prone to cleavage than C–C bonds. The sulfur compounds in

sulfur-abundant lacustrine samples can be detected by flash pyrolysis GC–MS (Sinninghe Damsté et al., 1989; Gelin et al., 1995; Grice et al., 2003). However, the sulfur-bonded compound series of aromatics, such as DBT, MDBTs, EDBTs, etc, were not detected in the present study, indicating that the abundance of organic sulfur compounds in samples the samples is extremely low or non-existent (Wang et al., 2018). Thus, it can be concluded that organic sulfur has no impact on the kinetics of these samples.

Above all, the kinetic results exhibit typical features of Type II kerogen and strong similarities can be observed in all samples. The slight difference in kinetics may be due to small differences in the kerogen composition. In view of this similarity, an average (typical) kinetic model of Type II brackish-lacustrine source rocks in the study area can be established based on the three samples. The average model is obtained by the weighted-average method (Peters et al., 2006; Wang et al., 2011): Samples with higher Rock-Eval S_2 are considered to exert more influence on the weighted kinetic parameters. Weighted proportional values, determined by the relative S_2 values of the samples, can be given to the kinetic parameters of each sample to combine their Ea and A values. In this way, a weighted kinetic model can be obtained. Fig. 7 compares the kinetic parameters derived from the three samples with those of the average kinetic model corrected by the weighted-average method. This method does not narrow or broaden the activation energy range but integrates the characteristics and reduces the difference of the three kinetic models. The average kinetic model is still dominated by Ea value of 52 kcal/mol (Fig. 7). This average kinetic model can be regarded as the typical kinetic model of the Type II brackish-lacustrine source rocks in the southern BS.

570 *5.4. Transformation of Type II kerogen from brackish lake*

571 The kinetic parameters of the samples from the southern BS present similar
572 characteristics, but the similarities or differences among the samples become more
573 obvious when the kinetic model is extrapolated to a geological heating rate, a common
574 practice in kinetic studies (Burnham et al., 1989; Schaefer et al., 1990; Dieckmann, 1998;
575 Lewan et al., 2006; Peters et al., 2006, 2018). The average geological heating rate in a
576 specified basin can be reasonably obtained from the time-temperature history (Welte et al.,
577 1997). According to studies of the thermal history in the southern BS (Sun et al., 2011;
578 Niu, 2012; Cheng et al., 2013), the average geological heating rate varies in the range
579 2.8–3.2 K/Ma. Therefore, the median value (3 K/Ma) is assumed to be the geological
580 heating rate in this study.

581 As shown in Fig. 8, the TR curves of liquid oil generation span a broad temperature
582 interval of 75–146 °C. TR values between 0.1 and 0.9 have been defined as the oil
583 generation window of source rocks (Pepper and Corvit, 1995). The oil generation window
584 can be divided into three stages according to the TR value (Houseknecht and Hayba, 1998):
585 early generation phase, main generation phase and late generation phase, corresponding to
586 TR of 0.10–0.25, 0.25–0.65 and 0.65–0.9, respectively. The samples in the study area have
587 entered the early generation phase when the geological temperature reached 90 °C. The
588 onset of the main generation phase corresponds to temperatures of 100–103 °C. This phase
589 ends at 125–129 °C. The late generation phase ends at geological temperatures of 138 °C.
590 As shown in Fig. 8, these TR curves show strong consistency among the samples. The
591 variations among TR curves are no more than 4 °C during the oil generation. Even for
592 replicate kinetic analyses (10 replicates) of the same sample (Green River shale), the

corresponding geological temperatures differed by up to 2.3 °C at a given TR (Peters et al., 2006). Therefore, variations of 4 °C in this study can be considered a very slight difference among TR curves, which reconfirm the similar kinetic characteristics of these samples. The TR evolution curve of the average kinetic model is located in the neutral area among the TR curves of the three samples (Fig. 8). The corresponding oil generation phase starts at 92 °C and ends at 137 °C, and the geological temperature of the main generation phase is between 102 and 127 °C. This study not only provides basic and reliable data for the modelling of source rocks and the evolution of oil generation, but also demonstrates that trace elements and flash pyrolysis-GC–MS are useful and necessary tools in kinetic studies of source rocks. In addition, the work in this paper establish the average kinetic model for Type II kerogens and can serve as a reference to lacustrine Type II kerogens in regions that share similar depositional environments with the southern Bohai Sea.

6. Conclusions

Closed-system pyrolysis of three Type II kerogens isolated from the mudstones in Ed_3, Es_{1-2}, and Es_3, southern Bohai Sea was performed to determine the kinetics of oil (C_{14+}) generation. These samples share similar palaeo-environments (hot and arid climates, anoxic conditions and brackish water in shallow to semi-deep lakes) and kerogen chemical composition (mainly sourced from lacustrine algae with relatively low contribution from land plants). The activation energy of the samples ranges from 44 to 52 kcal/mol with a frequency factor from 1.116×10^{14} to 1.274×10^{14} s^{-1}. Strong consistency exists in the kinetic parameters of the three samples. The consistencies become more obvious on the TR curves

of samples. The corresponding geological temperatures of the samples vary within just 4 °C at the given TR. Based on the close similarity in paleo-environment, kerogen chemical compositions and kinetic parameters between the samples, an average kinetic model of brackish-lacustrine source rocks in the southern Bohai Sea was established via the weighted-average method. The average kinetic model reduces the difference and integrates the characteristics of the three kinetic models. This model is still dominated by an activation energy of 52 kcal/mol. The geological temperature span of the oil generation phase for the average model is 92–137 °C.

Acknowledgements

This study was supported by grants from National Science and Technology Major Projects (Grant No. 2016ZX05024-002-007), Open fund of State Key Laboratory of Oil and Gas Reservoir Geology and Exploitation (Grant No. PLC20180305), National Science and Technology Major Projects (Grant No. 2016ZX05024-002-006), National Science and Technology Major Projects (Grant No. 2016ZX05027-002-006), and Independent Project of Key Laboratory of Coal Exploration and Comprehensive Utilization (Grant No. ZP2018-1). We are grateful to Associate Editor Michael Erdmann and two anonymous reviewers for their helpful comments on this paper.

Associate Editor–**Michael Erdmann**

References

Abbassi, S., Edwards, D.S., George, S.C., Volk, H., Mahlstedt, N., Horsfield, B., 2016.

639 Petroleum potential and kinetic models for hydrocarbon generation from the Upper
640 Cretaceous to Paleogene Latrobe Group coals and shales in the Gippsland Basin,
641 Australia. Organic Geochemistry 91, 54–67.
642 Adams, T.D., Haynes, J.R., Waker, C.T., 1963. Boron in Holocene illites of the Dovey Estuary,
643 Wales, and its relationship to palaeosalinity in cyclothems. Sedimentology 4, 189–195.
644 Alexandrine, N., Simon III, N., Gabriel, N., 2019. The late Pleistocene–Holocene
645 paleoclimate reconstruction in the Adamawa plateau (Central Cameroon) inferred
646 from the geochemistry and mineralogy of the Lake Fonjak sediments. Journal of
647 African Earth Sciences 150, 23–36.
648 Allen, M.B., Macdonald, D.I.M., Zhao, X., Vincent, S.J., Brouet-Menzies, C., 1997. Early
649 Cenozoic two-phase extension and late Cenozoic thermal subsidence and inversion of
650 the Bohai Basin, Northern China. Marine and Petroleum Geology 14, 951–972.
651 Allred, V.D., 1966. Kinetics of oil shale pyrolysis. Chemical Engineering Progress 62, 55–60.
652 Audino, M., Grice, K., Alexander, R., Kagi, R.I., 2002. Macrocyclic alkanes in crude oils
653 from the algaenan of *Botryococcus braunii*. Organic Geochemistry 33, 979–984.
654 Behar, F., Lewan, M.D., Lorant, F., Vandenbroucke, M., 2003. Comparison of artificial
655 maturation of lignite in hydrous and nonhydrous conditions. Organic Geochemistry 34,
656 575–600.
657 Behar, F., Roy, S., Jarvie, D., 2010. Organic geochemistry artificial maturation of a Type I
658 kerogen in closed system: Mass balance and kinetic modelling. Organic Geochemistry
659 41, 1235–1247.
660 Behar, F., Tang, Y., Liu, J., 1997a. Comparison of rate constants for some molecular tracers
661 generated during artificial maturation of kerogens: Influence of kerogen type. Organic

662 Geochemistry 26, 281–287.
663 Behar, F., Vandenbroucke, M., Tang, Y., Marquis, F., 1997b. Thermal cracking of kerogen in
664 open and closed systems: Determination of kinetic parameters and stoichiometric
665 coefficients for oil and gas generation. Organic Geochemistry 26, 321–339.
666 Braun, R.L., Burnham, A.K., 1987. Analysis of chemical reaction kinetics using a distribution
667 of activation energies and simpler models. Energy & Fuels 1, 153–161.
668 Burnham, A.K., 2017. Global Chemical Kinetics of Fossil Fuels. Springer, Switzerland.
669 Burnham, A.K., Braun, R.L., Gregg, H.R., Samoun, A.M., 1987. Comparison of methods for
670 measuring kerogen pyrolysis rates and fitting kinetic parameters. Energy & Fuels 1,
671 452–458.
672 Burnham, A.K., Crawford, R.W., Samoun, A.M., 1989. Pyrolysis of Argonne premium coals :
673 Activation energy distributions and related chemistry. Energy & Fuels 3, 42–55.
674 Burnham, A.K., Schmidt, B.J., Braun, R.L., 1995. A test of the parallel reaction model using
675 kinetic measurements on hydrous pyrolysis residues. Organic Geochemistry 23,
676 931–939.
677 Cao, H., Gip, W., Shan, X., Ma, L., Sun, P., 2015. Paleolimnological environments and
678 organic accumulation of the Nenjiang formation in the southeastern Songliao basin,
679 China. Oil Shale 32, 5–24.
680 Liu, C., Li, W., Wu, Z., Zhang, X., Chen, X., Li, C., 2016. Development characteristics of the
681 Cenozoic fault system and basin evolution of Bonan area in Bohai Sea. Geological
682 Journal of China Universities 22, 317–326.
683 Chen, Z., Jiang, C., 2015. A data driven model for studying kerogen kinetics with application
684 examples from Canadian sedimentary basins. Marine and Petroleum Geology 67,

795–803.

Chen, Z., Li, M., Cao, T., Ma, X., Li, Z., Jiang, Q., Li, Z., Jiang, C., 2017. Hydrocarbon generation kinetics of a heterogeneous source rock system: Example from the lacsutrine Eocene-Oligocene Shahejie Formation, Bohai Bay Basin. China. Energy & Fuels 31, 13291–13304.

Cheng, Y., Wu, Z., Li, W., Wang, Z., 2013. Thermal history of Paleogene source rocks in the Qingdong Sag, Bohai Bay Basin. Geological Journal of China Universities 19, 141–147.

Couch, E.L., 1971. Calculation of paleosalinities from boron and clay mineral data. American Association of Petroleum Geologists Bulletin 55, 1829–1837.

Derenne, S., Largeau, C., Behar, F., 1994. Low polarity pyrolysis products of Permian to recent *Botryococcus*-rich sediments: First evidence for the contribution of an isoprenoid algaenan to kerogen formation . Geochimica et Cosmochimica Acta 58, 3703–3711.

Dieckmann, V., 1998. Kinetics of petroleum generation and cracking by closed-system pyrolysis of Toarcian Shales. Fuel 77, 23–31.

Dieckmann, V., 2005. Modelling petroleum formation from heterogeneous source rocks: the influence of frequency factors on activation energy distribution and geological prediction. Marine and Petroleum Geology 22, 375–390.

Dieckmann, V., Horsfield, B., Schenk, H.J., 2000. Heating rate dependency of petroleum-forming reactions: Implications for compositional kinetic predictions. Organic Geochemistry 31, 1333–1348.

Dieckmann, V., Fowler, M., Horsfield, B., 2004. Predicting the composition of natural gas

708 generated by the Duvernay Formation (Western Canada Sedimentary Basin) using a
709 compositional kinetic approach. Organic Geochemistry 35, 845–862.
710 Dieckmann, V., Schenk, H.J., Horsfield, B., Welte, D.H., 1998. Kinetics of petroleum
711 generation and cracking by programmed-temperature closed-system pyrolysis of
712 Toarcian Shales. Fuel 77, 23–31.
713 Flaviano, C., Berre, F.L., Derenne, S., Largeau, C., Connan, J., 1994. First indications of the
714 formation of kerogen amorphous fractions by selective preservation. Role of
715 non-hydrolysable macromolecular constituents of Eubacterial cell walls. Organic
716 Geochemistry 22, 759–771.
717 Friedman, H.L., 1964. Kinetics of thermal degradation of char-forming plastics from
718 thermogravimetry. Application to a phenolic plastic. Journal of Polymer Science: Part
719 C 6, 183–195.
720 Fusetti, L., Behar, F., Bounaceur, R., Marquaire, P.M., Grice, K., Derenne, S., 2010a. New
721 insights into secondary gas generation from the thermal cracking of oil: Methylated
722 monoaromatics. A kinetic approach using 1,2,4-trimethylbenzene. Part I: A
723 mechanistic kinetic model. Organic Geochemistry 41, 146–167.
724 Fusetti, L., Behar, F., Grice, K., Derenne, S., 2010b. New insights into secondary gas
725 generation from the thermal cracking of oil: Part II: An empirical kinetic model.
726 Organic Geochemistry 41, 168–176.
727 Gao, X., Xiao, X., Zhao, B., Lu, H., Tang, Y., 2004. Petroleum generation history of Lower
728 Tertiary source rocks from the Bozhong Depression of the Bohaiwan Basin. Acta
729 Sedimentologica Sinica 22, 359–364.
730 Gelin, F., de Leeuw, J.W., Sinninghe Damsté, J.S., Derenne, S., Largeau, C., Metzger, P., 1994.

731 The similarity of chemical structures of soluble aliphatic polyaldehyde and insoluble
732 algaenan in the green microalga *Botryococcus braunii* race A as revealed by analytical
733 pyrolysis. Organic Geochemistry 21, 423–435.
734 Gelin, F., Sinninghe Damsté, J.S., Harrison, N.W., Maxwell, R.J., de Leeuw, J.W., 1995.
735 Molecular indicators for palaeoenvironmental change in a Messinian evaporitic
736 sequence (Vena del Gesso, Italy): III. Stratigraphic changes in the molecular structure
737 of kerogen in a single marl bed as revealed by flash pyrolysis. Organic Geochemistry
738 23, 555–566.
739 Greenwood, P.F., Brocks, J.J., Grice, K., Schwark, L., Jaraula, C.M.B., Dick, J.M., Evans,
740 K.A., 2013. Organic geochemistry and mineralogy. I. Characterisation of organic
741 matter associated with metal deposits. Ore Geology Reviews 50, 1–27.
742 Grice, K., Eiserbeck, C., 2013. The Analysis and Application of Biomarkers, Treatise on
743 Geochemistry: Second Edition, vol. 12. Elsevier, pp. 47-78..
744 Grice, K., Schouten, S., Blokker, P., Derenne, S., Largeau, C., Nissenbaum, A., Sinninghe
745 Damsté, J.S., 2003. Structural and isotopic analysis of kerogens in sediments rich in
746 free sulfurised *Botryococcus braunii* biomarkers. Organic Geochemistry 34, 471–482.
747 Guo, X., Xion, M., Zeng, Q., Xiao, X., 2008. Petroleum generation model of a sulfur-rich
748 kerogen from the Linnan Sag, the Bohai Bay Basin. Petroleum Geology & Experiment
749 30, 265–269.
750 Guo, X., Xiong, M., Zhou, Q., Tian, H., Xiao, X., 2009. Petroleum generation and expulsion
751 kinetics: A case study of the Shahejie Formation source rocks from Linnan Sag of
752 Huimin Depression. Acta Sedimentologica Sinica 27, 723–731.
753 Hao, F., Zhou, X., Zhu, Y., Yang, Y., 2009. Mechanisms for oil depletion and enrichment on

754 the Shijiutuo uplift, Bohai Bay Basin, China. American Association of Petroleum
755 Geologists Bulletin 93, 1015–1037.
756 Harris, N.B., Mnich, C.A., Selby, D., Korn, D., 2013. Minor and trace element and Re-Os
757 chemistry of the Upper Devonian Woodford Shale, Permian Basin, west Texas:
758 Insights into metal abundance and basin processes. Chemical Geology 356, 76–93.
759 He, M., Moldowan, J.M., Peters, K.E., 2018. Biomarkers: Petroleum. In: White, W. (Ed.),
760 Encyclopedia of Geochemistry, Springer Cham.
761 **DOI:** https://doi.org/10.1007/978-3-319-39193-9_170-1
762 Höld, I.M., Schouten, S., van der Gaast, S.J., Sinninghe Damsté, J.S., 2001. Origin of
763 prist-1-ene and prist-2-ene in kerogen pyrolysates. Chemical Geology 172, 201–212.
764 Holman, A.I., Grice, K., 2018. $\delta^{13}C$ of aromatic compounds in sediments, oils and
765 atmospheric emissions: A review. Organic Geochemistry 123, 27–37.
766 Horsfield, B., 1989. Practical criteria for classifying kerogens: Some observations from
767 pyrolysis-gas chromatography. Geochimica et Cosmochimica Acta 53, 891–901.
768 Houseknecht, D.W., Hayba, D.O., 1998. Modeling oil generation in the undeformed part of
769 the artict national wildlife refuge 1002 area. Alaska Open File Report 98-37, United
770 States Geological Survey.
771 Hsiao, L.Y., Graham, S.A., Tilander, N., 2004. Seismic reflection imaging of a major
772 strike-slip fault zone in a rift system: Paleogene structure and evolution of the Tan-Lu
773 fault system, Liaodong Bay, Bohai, offshore China. American Association of
774 Petroleum Geologists Bulletin 88, 71–97.
775 Huang, W., Meinschein, W.G., 1979. Sterols as ecological indicators. Geochimica et
776 Cosmochimica Acta 43, 739–745.

Huang, W., Zeng, L., Pan, C., Xiao, Z., Zhang, H., Huang, Z., 2019. Petroleum generation potentials and kinetics of coaly source rocks in the Kuqa Depression of Tarim Basin, Northwest China. Organic Geochemistry 133, 32–52.

Huang, Z., Liang, T., Zhan, Z.W., Zou, Y.R., Li, M., Peng, P., 2018. Chemical structure evolution of kerogen during oil generation. Marine and Petroleum Geology 98, 422–436.

Hunt, J.M., Lewan, M.D., Hennet, R.-C., 1991. Modelling oil generation with time–temperature index graphs based on the Arrhenius equation. American Association of Petroleum Geologists Bulletin 75, 795–807.

Jiang, Q., Wang, Y., Qin, J., Qin, W., Zhang, C., 2008. Kinetics of the hydrocarbon generation process of marine source rocks in South China. Petroleum Exploration and Development Development 37, 174–180.

Jones, B., Manning, D.A.C., 1994. Comparison of geochemical indices used for the interpretation of palaeoredox conditions in ancient mudstones. Chemical Geology 111, 111–129.

Kayode, A., Hasiah, W., Hail, M., Sarki, B.M., Azlan, K., Oluyemi, A., 2014. Trace elements geochemistry of kerogen in Upper Cretaceous sediments, Chad (Bornu) Basin, northeastern Nigeria: Origin and paleo-redox conditions. Journal of African Earth Sciences 100, 675–683.

Klomp, U.C., Wright, P.A., 1990. A new method for the measurement of kinetic parameters of hydrocarbon generation from source rocks. Organic Geochemistry 16, 49–60.

Kodner, R.B., Pearson, A., Summons, R.E., Knoll, A.H., 2008. Sterols in red and green algae: quantification, phylogeny, and relevance for the interpretation of geologic steranes.

800 Geobiology 6, 411–420.
801 Lafargue, E., Marquis, F., Pillot, D., 1998. Rock-Eval 6 applications in hydrocarbon
802 exploration, production, and soil contamination studies. Revue de l'Institut Francais
803 du Petrole 53, 421–437.
804 Landais, P., Michels, R., Poty, B., Monthioux, M., 1989. Pyrolysis of organic matter in
805 cold-seal pressure autoclaves. Experimental approach and applications. Journal of
806 Analytical and Applied Pyrolysis 16, 103–115.
807 Largeau, C., Derenne, S., Casadevall, E., Kadouri, A., Sellier, N., 1986. Pyrolysis of immature
808 Torbanite and of the resistant biopolymer (PRB A) isolated from extant alga
809 *Botryococcus braunii*. Mechanism of formation and structure of Torbanite. Organic
810 Geochemistry 10, 1023–1032.
811 Larter, S.R., Horsfield, B., 1993. Determination of structural components of kerogens by the
812 use of analytical pyrolysis methods. In: Engel, M.H., Macko, S.A. (Eds.), Organic
813 Geochemistry, Springer, New York, pp. 271–287.
814 Larter, S.R., Solli, H., Douglas, A.G., de Lange, F., de Leeuw, J.W., 1979. Occurrence and
815 significance of prist-1-ene in kerogen pyrolysates. Nature 279, 405–408.
816 Lewan, M.D., 1998. Sulfur-radical control on rates of natural petroleum formation. Nature
817 391, 164–166.
818 Lewan, M.D., Kotarba, M.J., Curtis, J.B., Wiecław, D., Kosakowski, P., 2006. Oil-generation
819 kinetics for organic facies with Type-II and -IIS kerogen in the Menilite Shales of the
820 Polish Carpathians. Geochimica et Cosmochimica Acta 70, 3351–3368.
821 Lewan, M.D., Spiro, B., Illich, H., Raiswell, R., Mackenzie, A.S., Durand, B., Comet, P.A.,
822 Berner, R.A., de Leeuw, J.W., 1985. Evaluation of petroleum generation by hydrous

pyrolysis experimentation. Mathematical and Physical Sciences 315, 123–134.

Li, Y., 2015. Main controlling factors for the development of high quality lacustrine hydrocarbon source rocks in offshore China. China Offshore Oil and Gas 27, 1–9.

Li, Y., He, D., 2014. Evolution of tectonic-depositional environment and prototype basins of the Early Jurassic in Sichuan Basin and adjacent areas. Acta Petrolei Sinica 35, 219–232.

Liang, H., Xu, F., Xu, G., Yuan, H., Huang, S., Wang, Y., Wang, L., Fu, D., 2019. Geochemical characteristics and origins of the diagenetic fluids of the Permian Changxing Formation calcites in the Southeastern Sichuan Basin: Evidence from petrography, inclusions and Sr, C and O isotopes. Marine and Petroleum Geology 103, 564–580.

Liu, C., Li, W., Wu, Z., Zhang, X., Chen, X., Li, C., 2016. Development characteristics of the Cenozoic fault system and basin evolution of Bonan area in Bohai Sea. Geological Journal of China Universities 22, 317–326.

Liu, L., Jiang, Z., Zhong, N., Zheng, F., 2009. Hydrocarbon-generating dynamic characteristics of Paleogene source rocks in Western Depression, Liaohe Basin. Earth Science–Journal of China University of Geosciences 34, 799–805.

Liu, Y., He, K., Li, X., Xu, H., Zhang, J., Hu, S., Wang, G., Fan, Z., 2016. Hydrocarbon generation kinetics and the efficiency of petroleum expulsion of lacustrine source rocks: Taking the Qingshankou Formation in the Songliao Basin as an example. Geoscience 30, 627–634.

Lu, H., Chen, T., Liu, J., Peng, P., Lu, Z., Ma, Q., 2010. Yields of H_2S and gaseous hydrocarbons in gold tube experiments simulating thermochemical sulfate reduction

reactions between $MgSO_4$ and petroleum fractions. Organic Geochemistry 41, 1189–1197.

Mao, R., Mi, J., Zhang, S., He, K., 2012. Study on the hydrocarbon generation characteristics of differernt coaly source rocks by gold-tube pyrolysis experiments. Natural Gas Geoscience 23, 1127–1134.

Monthioux, M., Landais, P., Monin, J.-C., 1985. Comparison between natural and artificial maturation series of humic coals from the Mahakam delta, Indonesia. Organic Geochemistry 8, 275–292.

Monthioux, M., Landais, P., Durand, B., 1986. Comparison between extracts from natural and artificial maturation series of Mahakam delta coals. Organic Geochemistry 10, 299–311.

Niu, C., 2012. Tectonic evolution and hydrocarbon accumulation of Laizhouwan depression in southern Bohai Sea. Oil and Gas Geology 33, 424–431.

Niu, C., Jin, Q., Li, P., Zhang, R., Cheng, F., Wu, K., 2018. Kinetic study on oil and gas generation from Paleogene source rocks in Liaodong Bay area, Northern China. Marine Origin Petroleum Geology 23, 91–96.

Pei, C., Zhou, Z., 1989. A study of the influence of characteristics of kerogen on oil-gas generation. Geochimica 4, 322–333.

Pepper, A.S., Corvit, P.J., 1995. Simple kinetic models of petroleum formation. Part I: oil and gas generation from kerogen. Marine and Petroleum Geology 12, 291–319.

Peters, K.E., Burnham, A.K., Walters, C.C., Schenk, O., 2018. Guidelines for kinetic input to petroleum system models from open-system pyrolysis. Marine and Petroleum Geology 92, 979–986.

869 Peters, K.E., Walters, C.C., Mankiewicz, P.J., 2006. Evaluation of kinetic uncertainty in
870 numerical models of petroleum generation. American Association of Petroleum
871 Geologists Bulletin 90, 387–403.
872 Reynolds, J.G., Burnham, K., Mitchell, T.O., 1995. Programmed temperature micropyrolysis.
873 Organic Geochemistry 23, 109–120.
874 Saxby, J.D., 1970. Isolation of kerogen in sediments by chemical methods. Chemical
875 Engineering Science 6, 173–184.
876 Schaefer, R.G., Schenk, H.J., Hardelauf, H., Harms, R., 1990. Determination of gross kinetic
877 parameters for petroleum formation from Jurassic source rocks of different maturity
878 levels by means of laboratory experiments. Organic Geochemistry 16, 115–120.
879 Schenk, H.J., Dieckmann, V., 2004. Prediction of petroleum formation: the influence of
880 laboratory heating rates on kinetic parameters and geological extrapolations. Marine
881 and Petroleum Geology 21, 79–95.
882 Sinninghe Damsté, J.S., Eglinton, T.I., de Leeuw, J.W., Schenck, P.A., 1989. Organic sulphur
883 in macromolecular sedimentary organic matter: I. Structure and origin of
884 sulphur-containing moieties in kerogen, asphaltenes and coal as revealed by flash
885 pyrolysis. Geochimica et Cosmochimica Acta 53, 873–889.
886 Sinninghe Damsté, J.S., de las Heras, F.X.C., Bergen, P.F., de Leeuw, J.W., 1993.
887 Characterization of Tertiary Catalan lacustrine oil shales: Discovery of extremely
888 organic sulphur-rich Type I kerogens. Geochimica et Cosmochimica Acta 57,
889 389–415.
890 Sun, H., Zhou, X., Peng, W., Zou, H., Yang, B., He, D., Zeng, X., 2011. Late-stage
891 hydrocarbon accumulation and enrichment in the Huanghekou Sag, southern Bohai

892 Sea. Petroleum Exploration and Development 38, 307–313.
893 Sun, M., Mi, J., Feng, Z., Li, Q., Zhang, J., Liu, Y., 2015. Comparison of the characteristics of
894 hydrocarbons generated by Type Ⅰ of organic matter using two different experiment
895 methods in Gold Tube System. Natural Gas Geoscience 26, 1156–1164.
896 Sweeney, J.J., Burnham, A.K., 1990. Evaluation of a simple model of vitrinite reflectance
897 based on chemical kinetics. American Association of Petroleum Geologists Bulletin 74,
898 1559–1570.
899 Tegelaar, E.W., Noble, R.A., 1994. Kinetics of hydrocarbon generation as a function of the
900 molecular structure of kerogen as revealed by pyrolysis-gas chromatography. Organic
901 Geochemistry 22, 543–574.
902 Tissot, B.P., Pelet, R., Ungerer, P., 1987. Thermal history of sedimentary basins, maturation
903 Indices, and kinetics of oil and gas generation. American Association of Petroleum
904 Geologists Bulletin 71, 1445–1466.
905 Tissot, B.P., Welte, D.H., 1984. Petroleum Formation and Occurrence. Springer-Verlag, Berlin,
906 Heidelberg, New York, Tokyo.
907 Tribovillard, N., Algeo, T.J., Lyons, T., Riboulleau, A., 2006. Trace metals as paleoredox and
908 paleoproductivity proxies: An update. Chemical Geology 232, 12–32.
909 Ungerer, P., Durand, B., Behar, F., 1990. State of the art of research in kinetic modelling of oil
910 formation and expulsion. Organic Geochemistry 16, 1–25.
911 van Graas, G., de Leeuw, J.W., Schenck, P.A., Haverkamp, J., 1981. Kerogen of Toarcian
912 shales of the Paris Basin. A study of its maturation by flash pyrolysis techniques.
913 Geochimica et Cosmochimica Acta 45, 2465–2474.
914 Volkman, J.K., 1986. A review of sterol markers for marine and terrigenous organic matter.

915 Organic Geochemistry 9, 83–99.
916 Volkman, J.K., 1988. Biological marker compounds as indicators of the depositional
917 environments of petroleum source rocks. Geological Society Special Publication 40,
918 103–122.
919 Volkman, J.K., Barrett, S.M., Dunstan, G.A., Jeffrey, S.W., 1994. Sterol biomarkers for
920 microalgae from the green algal class Prasinophyceae. Organic Geochemistry 21,
921 1211–1218.
922 Wang, F., Guo, S., 2019a. Shale gas content evolution in the Ordos Basin. International
923 Journal of Coal Geology 211, 1–13.
924 Wang, F., Guo, S., 2019b. Influential factors and model of shale pore evolution: A case study
925 of a continental shale from the Ordos Basin. Marine and Petroleum Geology 102,
926 271–282.
927 Wang, F., Liu, X., Deng, X., Li, Y., Tian, J., Li, S., You, J., 2017. Geochemical characteristics
928 and environmental implications of trace elements of Zhifang Formation in Ordos
929 Basin. Acta Sedimentologica Sinica 35, 1265–1271.
930 Wang, J., Wang, Q., Wang, F., Liu, X., Pan, W., , 2017. Gold tube pyrolysis study of source
931 rock hydrocarbon generation in Bozhong area, offshore Bohai Bay Basin. Petroleum
932 Geology and Experiment 39, 423–430.
933 Wang, J., Wang, Q., Wang, F., Zhen, H., Chen, R., 2018. Hydrocarbon generation kinetics of
934 source rocks under different pyrolysis conditions in Bozhong area. Geological Science
935 & Technology Information 37, 108–114.
936 Wang, J., Xiao, X., Guo, R., Lu, H., Gao, X., 2003. Study on the hydrocarbon generation
937 kinetics of source rocks from the Dongying depression, Bohai Bay Basin. Petroleum

938 Geology & Experiment 25, 1–18.
939 Wang, L., Zhou, X., Niu, C., Yang, B., 2011. The effect of structure evolution on hydrocarbon
940 accumulation in Laizhouwan depression, Bohai Bay. Chinese Journal of Geology 46,
941 838–846.
942 Wang, M., Lu, S., Xue, H., 2011. Kinetic simulation of hydrocarbon generation from
943 lacustrine type I kerogen from the Songliao Basin: Model comparison and geological
944 application. Marine and Petroleum Geology 28, 1714–1726.
945 Wang, Q., Pan, S., Bai, J., Chi, M., Cui, D., Wang, Z., Liu, Q., Xu, F., 2018. Experimental and
946 dynamics simulation studies of the molecular modeling and reactivity of the Yaojie oil
947 shale kerogen. Fuel 230, 319–330.
948 Wang, Q., Zou, H., Hao, F., Zhu, Y., Zhou, X., Wang, Y., Tian, J., Liu, J., 2014. Modeling
949 hydrocarbon generation from the Paleogene source rocks in Liaodong Bay, Bohai Sea:
950 A study on gas potential of oil-prone source rocks. Organic Geochemistry 76,
951 204–219.
952 Wei, W., Algeo, T.J., Lu, Y., Lu, Y.C., Liu, H., Zhang, S., Peng, L., Zhang, J., Chen, L., 2018.
953 Identifying marine incursions into the Paleogene Bohai Bay Basin lake system in
954 northeastern China. International Journal of Coal Geology 200, 1–17.
955 Wei, Z., Zou, Y., Cai, Y., Wang, L., Luo, X., 2012. Kinetics of oil group-type generation and
956 expulsion: An integrated application to Dongying Depression, Bohai Bay Basin, China.
957 Organic Geochemistry 52, 1–12.
958 Wei, Z., Wang, Y., Wang, G., Sun, Z., Zhang, T., Xu, L., Ma, X., He, W., 2018.
959 Paleoenvironmental conditions of organic-rich Upper Permian Dalong Formation
960 shale in the Sichuan Basin, southwestern China. Marine and Petroleum Geology 91,

152–162.

Welte, D., Horsfield, B., Baker, D., 1997. Petroleum and Basin Evolution. Spinger.

Wen, H., Hou, Z., Lin, X., 2014. Depositional systems of the Neogene Shahejie Formation in the Qingdong Depression. Sedimentary Geology and Tethyan Geology 34, 20–30.

Wood, D.A., 2018. Kerogen conversion and thermal maturity modelling of petroleum generation: Integrated analysis applying relevant kerogen kinetics. Marine and Petroleum Geology 89, 313–329.

Wu, K., Jiang, X., Sun, H., 2015. Model of lacustrine source rocks in offshore oil kitchen sags: A case study of Paleogene in Huanghekou Sag. Geological Science & Technology Information 34, 63–70.

Wu, Z., Zhou, Y., 2000. Using the characteristic elements from meteoritic dust in strata to calculate sedimentation Rate. Acta Sedimentologica Sinica 18, 395–399.

Xiang, B., Li, E., Gao, X., Wang, M., Wang, Y., Xu, H., Huang, P., Yu, S., Liu, J., Zou, Y., Pan, C., 2016. Petroleum generation kinetics for Permian lacustrine source rocks in the Junggar Basin, NW China. Organic Geochemistry 98, 1–17.

Xin, Y., Ren, J., Li, J., 2013. Control of tectonic-paleogeomorphology on deposition: A case from the Shahejie Formation Sha 3 member, Laizhouwan Sag, southern Bohai Sea. Petroleum Exploration and Development 40, 325–332.

Xu, F., Liang, J., Xu, G., Yuan, H., Liu, Y., 2018. Genetic mechanisms and distribution characteristics of overpressures in the Paleogene reservoirs of the Bohai Bay Basin, East China. Energy Exploration and Exploitation 36, 388–413.

Yan, K., Zuo, Y., Yang, M., Zhou, Y., Zhang, Y., Wang, C., Song, R., Feng, R., Feng, Y., 2019. Kerogen pyrolysis experiment and hydrocarbon generation kinetics in the Dongpu

984 Depression, Bohai Bay Basin, China. Energy & Fuels 33, 8511–8521.
985 Yang, B., Zeng, X., Wang, G., Sun, H., 2011. Predominant factors of reservoir forming in
986 Laizhouwan Sag. Journal of Chongqing University of Science and Technology
987 (Natural Sciences Edition) 13, 6–10.
988 Ye, C., Yang, Y., Fang, X., Zhang, W., 2016. Late Eocene clay boron-derived paleosalinity in
989 the Qaidam Basin and its implications for regional tectonics and climate. Sedimentary
990 Geology 346, 49–59.
991 Zhang, C., Gao, A., Liumzhe, Huang, J., Yang, Y., Zhang, Y., 2011. Study of character on
992 sedimentary water and palaeoclimate for Chang7 oil layer in Ordos Basin. Natural Gas
993 Geoscience 22, 582–587.
994 Zhang, D., Huang, D., Li, J., Zhang, Y., 1983. Kinetic features of thermo-degradation of
995 kerogens in oil shales and their geochemical significances. Oil and Gas Geology 4,
996 383–393.
997 Zhang, X., Wu, Z., Zhou, X., Niu, C., Li, W., Ren, J., Zhang, J., 2017. Cenozoic tectonic
998 characteristics and evolution of the southern Bohai Sea. Geotectonica et Metallogenia
999 41, 50–60.
1000 Zhang, Z., Volkman, J.K., Greenwood, P.F., Hu, W., Qin, J., Borjigin, T., Zhai, C., Liu, W.,
1001 2014. Flash pyrolysis of kerogens from algal rich oil shales from the Eocene Huadian
1002 Formation, NE China. Organic Geochemistry 76, 167–172.
1003 Zhou, H., Wang, Z., Cui, X., Lei, Z., 1999. Stratigraphic sequence of the Middle
1004 Neoproterozoic in the southern of North China platform. Geology Press, Beijing.
1005 Zhou, Q., Lu, Y., Li, S., Wang, H., 1997. The missing time calculation of the hiatus surface –
1006 A case study of the Upper Permian reefs section at the platform margin, Ziyun,

Guizhou. Acta Geologica Sinica 71, 7–17.

Zhu, G., Hu, W., Song, L., Liu, B., 2015. Quaternary activity along the Tan-Lu fault zone in the Bohai Bay, East China: Evidence from seismic profiles. Journal of Asian Earth Sciences 114, 5–17.

Zhu, G., Qiang, J., Dai, J., Zhang, S., Zhang, L., Zhang, Y., 2005. Composite hydrocarbon generation system: An important concept for source rock evaluation and hydrocarbon prediction in rift lacustrine basin. Chinese Journal of Geology 1, 133–144.

Zhuang, X., Zou, H., Yang, Y., Sun, H., 2010. Development mechanism of lacustrine source rocks in Yellow River. Science & Technology Review 28, 48–54.

Figure captions

Fig. 1. (a) Simplified geological map of the Bohai Sea (after Xu et al., 2018); (b) Detailed geological map of the study area (modified from Zhang et al., 2017); (c) C_{ro}ss section showing the structural framework of the study area (after Zhang et al., 2017). The full names of the abbreviations in this figure are as follows: Q (Quaternary), N*m* (Minghuazhen Formation), N*g* (Guantao Formation), E*d* (Dongying Formation), Es_1 (First member of Shahejie Formation), Es_2 (Second member of Shahejie Formation), Es_3 (Third member of Shahejie Formation), Es_4 (Fourth member of Shahejie Formation), E*k* (Kongdian Formation).

Fig. 2. General Cenozoic stratigraphy of the study area (modified from Xu et al., 2018 and Wei et al., 2018). Form.= Formation; Symb.= Symbol.

Fig. 3. (a) HI vs Tmax diagram of the samples; (b) HI vs OI diagram of the samples

Fig. 4. (a–c) correspond to the TICs of pyrolysates from sample D3, S1 and S3 at 650 °C; (d–f) are the combined mass fragmentograms (*m*/*z* 78+91+128+142+156) of sample D3, S1 and S3, showing the distribution of aromatics in pyrolysates; circles: *n*-alkanes; triangles: *n*-alkenes; squares: unresolved compounds; C_n = alkane/ene doublets; B= benzene; T= toluene; EtB= ethylbenzene; mXy= m-xylene; pXy= para-xylene; oXy= ortho-xylene; PrB= propylbenzene; BuB= butylbenzene; MeN= methylnaphthalene; EtN= ethylnaphthalene; DimeN= dimethylnaphthalene; AlB= long chain alkyl benzenes; (g), (h) and (f) are the mass fragmentograms (*m*/*z* 217) of sample D3, S1 and S3, exhibiting the sterane distribution.

Fig. 5. Cumulative oil (C_{14+} fraction) yields with increasing temperature in pyrolysis experiments (a) Cumulative C_{14+} yields at heating rate of 20 °C/h; (b) Cumulative C_{14+} yields at heating rate of 2 °C/h;

Fig. 6. Best curve fittings and the kinetic parameter sets for the C_{14+} fraction (a–c) represent the fitting curves and measured TR of sample D3, S1, S3, respectively; (d–f) are the kinetic parameters (distribution of activation energies and frequency factor) of sample D3, S1, S3, respectively.

Fig. 7. Comparison of activation energies between the average kinetic model and samples in the southern Bohai Sea

1053 **Fig. 8**. TR evolution curves of kinetic models in the southern Bohai Sea

1054

Table 1
Geochemical characteristics of samples

Sample	D3	S1	S3
Well Name	HHK25-2-A	HHK25-2-A	LZW10-3-A
Depth (m)	2015-2030	2080-2095	2540-2555
Layer	Ed_3	Es_1	Es_3
TOC (wt%) [a]	3.3	2.8	4.3
HI (mg/g)[a]	613	601	559
OI (mg/g)[a]	33.6	28.3	20.1
S_2 (mg/g)[a]	20.1	16.9	24.0
S_3 (mg/g)[a]	1.1	0.79	0.86
T_{max} (°C)[a]	427	427	431
Mean %Ro [a]	0.39%	0.38%	0.37%
TOC (wt%) [b]	24.3	25.6	34.0

Note: “a” represents the original rock samples; “b” denotes kerogen samples

Table 2
Classification standard of paleo-environment

	Classification standard					Reference
Paleoclimate	Warm and humid climate Sr/Cu<10			Hot and arid climate Sr/Cu>10		Tian and Zhang (2015)
Pa1eoredox	Oxic V/V+Ni<	Dysoxic 0.46<V/V+Ni<0.6		Anoxic 0.54<V/V+Ni<0.82	Euxinic V/V+Ni>0.84	Hatch and Leventhal (1992)
Paleosalinity	Fresh water	Brackish water (Mixohaline)			Euhaline water	Hyperhaline water	Venice System (1958)
		Oligohaline	Mesohaline	Polyhaline		
	0–0.5 ppt	0.5–5 ppt	5–18 ppt	18-30 ppt	30–40 ppt	>40 ppt	
Paleowater depth	Shore	Shallow lake		Semi-deep	Deep lake	Wang (2011) Yang et al. (2015)
	0–5 m	5–30 m		30–50 m	>50 m	

Table 3
Trace element content and calculation of paleo-water depth

Sample name	V (μg/g)	Co (μg/g)	Ni (μg/g)	Cu (μg/g)	Sr (μg/g)	La (μg/g)	B (μg/g)	V/(V+Ni)	Sr/Cu	SR_L (mm/y)	SR (mm/y)	D (m)
D3	99.9	14.4	36.9	39.5	768	45.8	40.2	0.73	19.4	0.225	0.51	27
S1	89.3	15.0	35.6	35.3	734	45.9	46.8	0.71	20.8	0.225	0.47	30
S3	99.9	16.0	42.3	34.7	594	40.4	35.3	0.70	17.1	0.225	0.40	38

Note: SR_L range of normal lacustrine mudstone is between 0.15 and 0.3 mm/y (Zhang et al., 2011). As we do not have the accurate SR_L data, the middle value of the SR_L range (i.e. 0.225 mm/y) is assumed to be the SR_L in this study. D refers to the water depth (m).

Table 4
Results of XRD and calculation of paleosalinity

Sample name	Clay content (%)	Clay mineral content (%)						B (μg/g)	$B_{correct}$ (μg/g)	B_{clay} (μg/g)	B_k (μg/g)	S_p ppt
		I	K	C	I/S (S%)	I'	S'					
D3	48.7	27.0	7.0	1.0	65.0 (40)	66.0	26.0	40.2	22.2	45.6	14.1	6.5
S1	54.9	29.0	13.0	0.0	58.0 (40)	63.8	23.2	46.8	28.8	52.5	16.7	7.4
S3	51.8	35.0	6.0	2.0	57.0 (40)	69.2	22.8	35.3	17.3	33.4	10.2	5.0

Note: I - illite; K - kaolinite; Ch - chlorite; S - smectite; I'- calculated illite; S'- calculated smectite; B- measured boron abundance in rock sample; $B_{correct}$- corrected boron abundance in rock sample in which inherited B is subtracted ($B_{correct} = B_{rock} - B_{inherited}$); B_{clay}- boron abundance in clay fraction ($B_{clay} = B_{correct}$/Clay mineral content); B_k - the abundance of boron absorbed in kaolinite; S_p – palaeosalinity in parts per thousand.

Table 5

Parameters for analysis of the pyrolysate composition

Number	Parameter	Sample D3	Sample S1	Sample S3
1	C_6–C_{19} (aliphatic)/C_6–C_{29} (aliphatic)	0.68	0.65	0.67
2	C_{20}–C_{29} (aliphatic)/C_6–C_{29} (aliphatic)	0.32	0.35	0.33
3	Toluene/*n*-C_8 (alkane + alkene)	2.30	2.45	2.72
4	Toluene/Total monoaromatics	0.42	0.43	0.47
5	Benzene/Total monoaromatics	0.10	0.24	0.16
6	Prist-1-ene/*n*-C_{17} (alkane + alkene)	0.47	0.38	0.34

Note: Parameters are calculated from peak areas in mass fragmentograms for *m*/*z* 85 (alkanes), *m*/*z* 83 (alkenes), *m*/*z* 78 (benzene), *m*/*z* 91 (toluene) and *m*/*z* 91 (monoaromatics); Aliphatics = *n*-alkanes + *n*-alkenes.

Table 6

Liquid hydrocarbon products of immature kerogens at different heating rates and temperatures

Heating rate (°C/h)	Temperature (°C)	C_{14+} (mg/g TOC)		
		Sample D3	Sample S1	Sample S3
20	330	168	168	166
	340	226	216.71	216
	350	287	270.68	286
	360	345	*	354
	370	386	369	411
	380	427	419	467
	390	458	456	523
	400	432	438	487
	410	376	357	410
	420	339	300	321
	430	286	255	258
	440	242	197	185
2	290	133	125	130
	300	177	172	185
	310	225	218	232
	320	285	273	290
	330	339	324	353
	340	407	376	414
	350	447	441	485
	360	425	427	466
	370	389	351	427
	380	337	300	362
	390	293	251	291
	400	258	178	223

Note: Easy%Ro values in this table are calculated according to the method proposed by Sweeney and Burnham (1990). "*" in this table means the data were not obtained because of leakage of the gold tube during pyrolysis.

Table 7

Kinetic parameters for oil generation of source rock in the southern Bohai Sea

Sample	D3	S1	S3	Average model
Frequency factor (S^{-1})	1.121×10^{14}	1.116×10^{14}	1.274×10^{14}	1.180×10^{14}
Activation energy Ea (kcal/mol)	Reaction (%)	Reaction (%)	Reaction (%)	Reaction (%)
44	0.00	0.00	0.01	0.00
45	0.00	0.00	0.00	0.00
46	6.96	3.78	0.4	3.50
47	16.01	18.09	19.59	17.99
48	0.00	0.00	0.00	0.00
49	22.4	29.22	20.27	23.45
50	12.77	0.00	9.03	7.76
51	0.00	0.00	0.00	0.00
52	41.86	48.9	50.69	47.28
Average of Ea (kcal/mol)	49.85	50.00	50.20	50.03

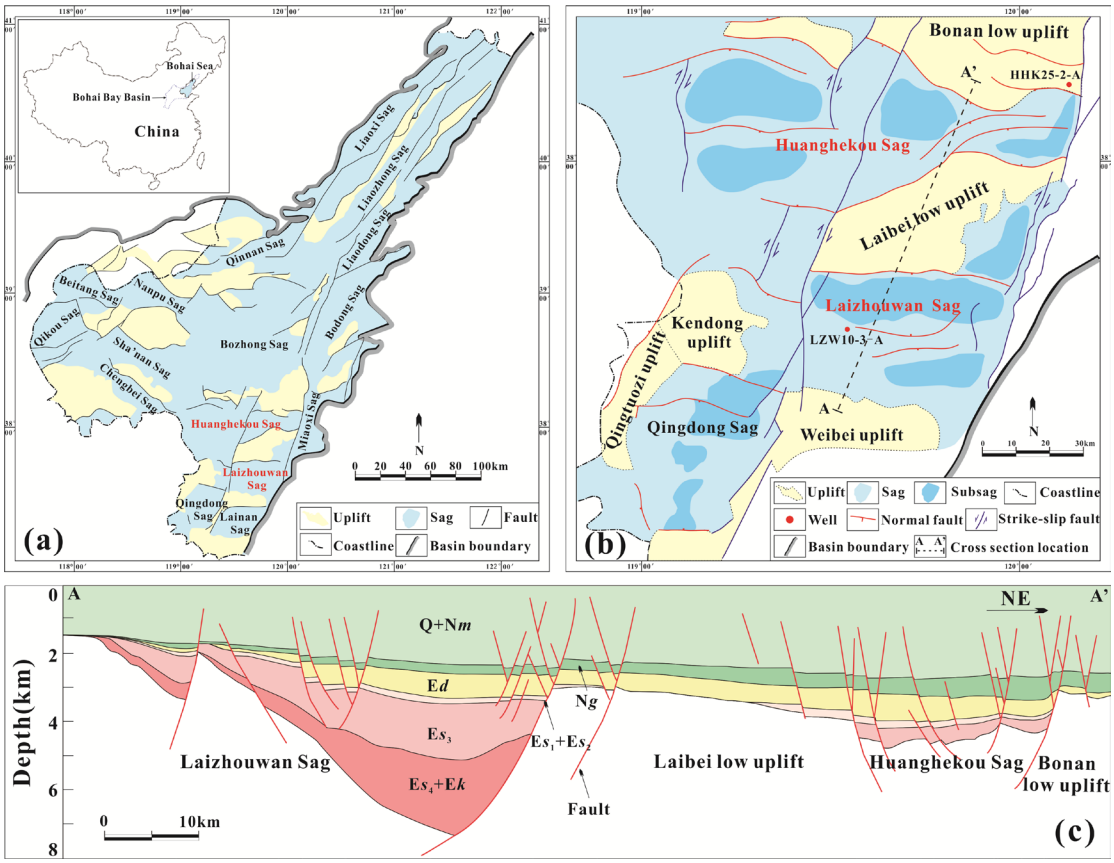
Bohai Sea
Bohai Bay Basin
China
Liaoxi Sag
Liaozhong Sag
Liaodong Sag
Qinnan Sag
Beitang Sag
Nanpu Sag
Qikou Sag
Sha'nan Sag
Chengbei Sag
Bozhong Sag
Bodong Sag
Miaoxi Sag
Huanghekou Sag
Laizhouwan Sag
Qingdong Sag
Lainan Sag
0 20 40 60 80 100km
Uplift
Sag
Fault
Coastline
Basin boundary
(a)
Bonan low uplift
A'
HHK25-2-A
Huanghekou Sag
Laibei low uplift
Laizhouwan Sag
Kendong uplift
LZW10-3-A
Qingtuozi uplift
A
Qingdong Sag
Weibei uplift
0 10 20 30km
Uplift
Sag
Subsag
Coastline
Well
Normal fault
Strike-slip fault
Basin boundary
Cross section location
(b)
A
NE
A'
Depth(km)
0
2
4
6
8
Q+Nm
Ed
Ng
Es3
Es1+Es2
Es4+Ek
Laizhouwan Sag
Laibei low uplift
Huanghekou Sag
Bonan low uplift
Fault
0 10km
(c)

Fig. 1

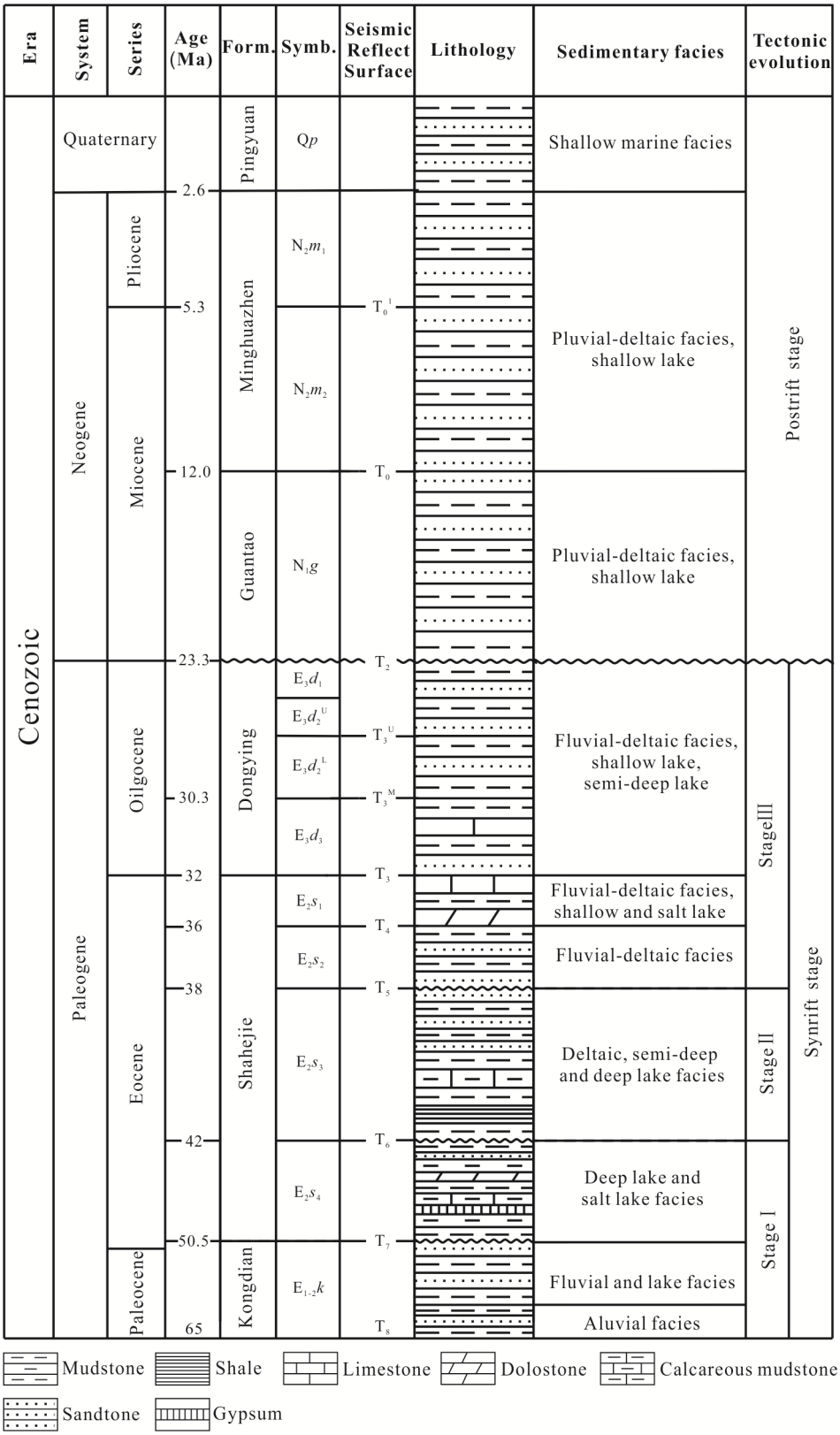
Era
System
Series
Age (Ma)
Form.
Symb.
Seismic Reflect Surface
Lithology
Sedimentary facies
Tectonic evolution
Cenozoic
Quaternary
Neogene
Paleogene
Pliocene
Miocene
Oilgocene
Eocene
Paleocene
2.6
5.3
12.0
23.3
30.3
32
36
38
42
50.5
65
Pingyuan
Minghuazhen
Guantao
Dongying
Shahejie
Kongdian
Qp
N2m1
N2m2
N1g
E3d1
E3d2U
E3d2L
E3d3
E2s1
E2s2
E2s3
E2s4
E1-2k
T0U
T0
T2
T3U
T3M
T3
T4
T5
T6
T7
T8
Shallow marine facies
Pluvial-deltaic facies, shallow lake
Pluvial-deltaic facies, shallow lake
Fluvial-deltaic facies, shallow lake, semi-deep lake
Fluvial-deltaic facies, shallow and salt lake
Fluvial-deltaic facies
Deltaic, semi-deep and deep lake facies
Deep lake and salt lake facies
Fluvial and lake facies
Aluvial facies
Postrift stage
StageIII
StageII
Stage I
Synrift stage
Mudstone
Shale
Limestone
Dolostone
Calcareous mudstone
Sandtone
Gypsum

Fig. 2

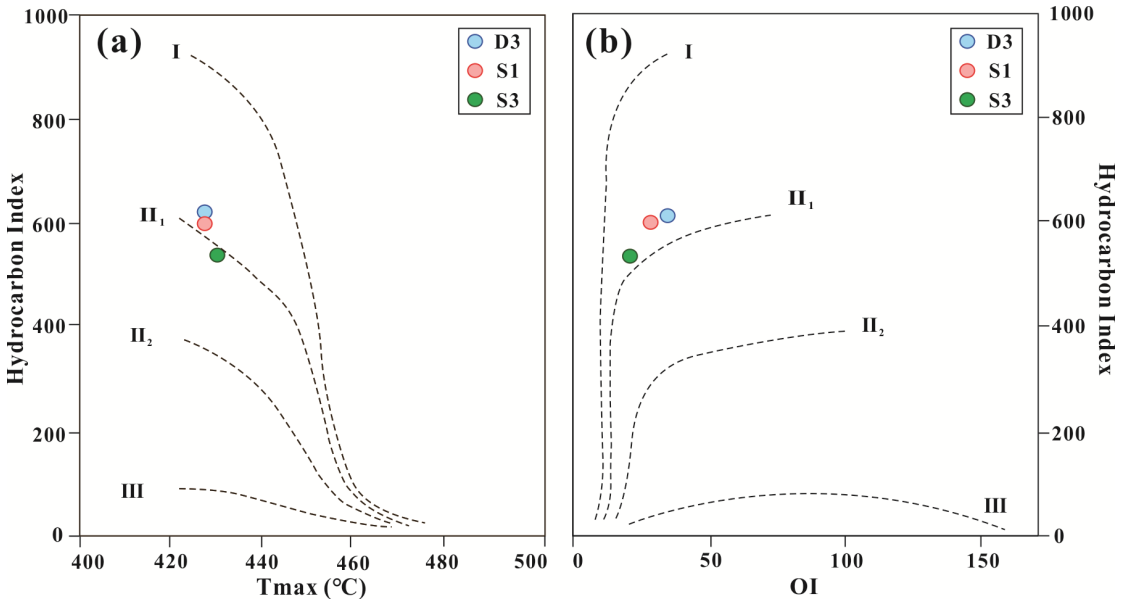
(a)
(b)
D3
S1
S3
I
II1
II2
III
Hydrocarbon Index
Tmax (℃)
OI
1000
800
600
400
200
0
400
420
440
460
480
500
0
50
100
150

Fig. 3

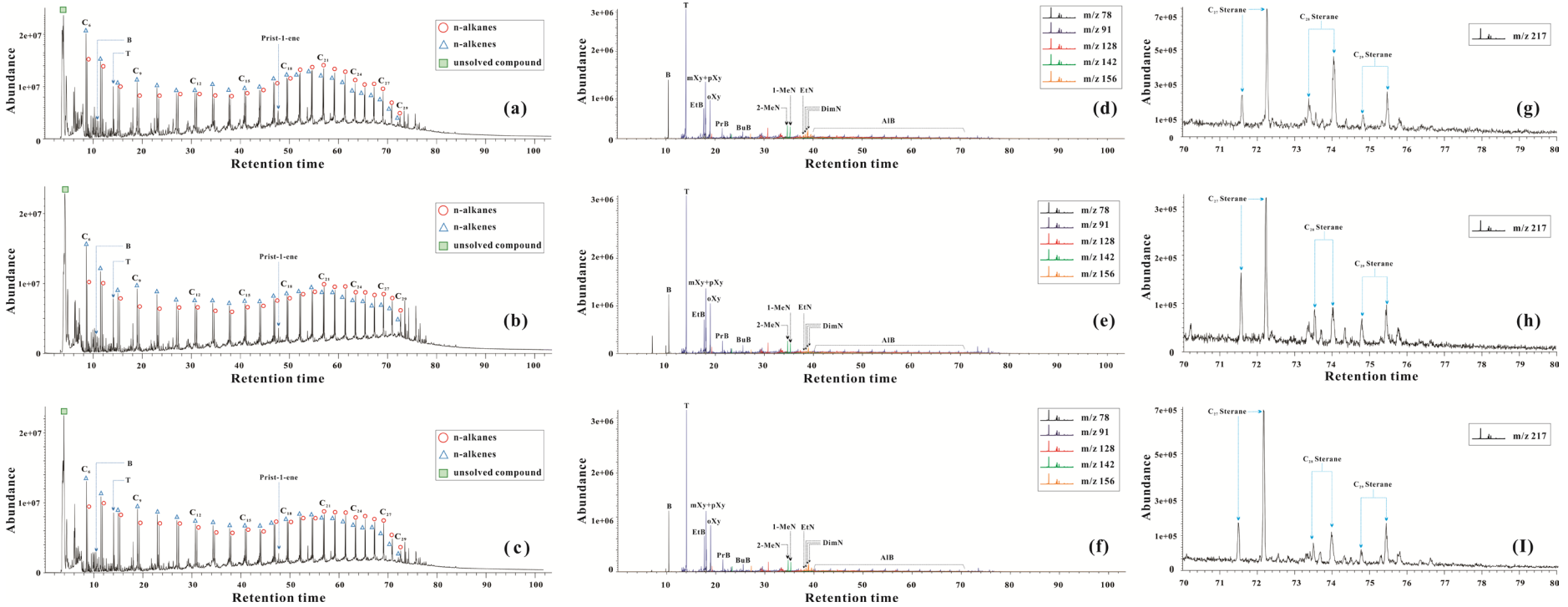
n-alkanes
n-alkenes
unsolved compound
Abundance
Retention time
Prist-1-ene
B
T
(a)
(b)
(c)
m/z 78
m/z 91
m/z 128
m/z 142
m/z 156
mXy+pXy
oXy
EtB
PrB
BuB
1-MeN
EtN
2-MeN
DimN
AlB
(d)
(e)
(f)
m/z 217
(g)
(h)
(I)

Fig. 4

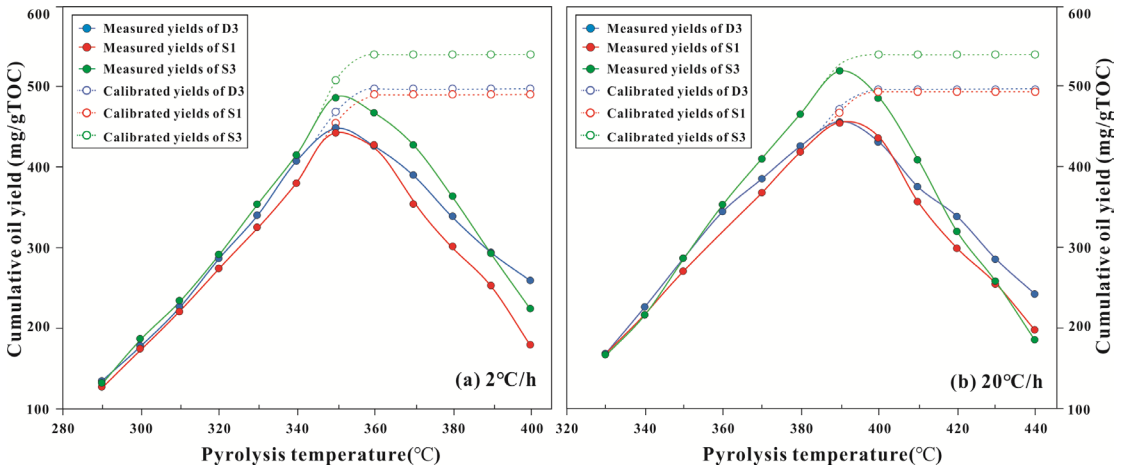
Measured yields of D3
Measured yields of S1
Measured yields of S3
Calibrated yields of D3
Calibrated yields of S1
Calibrated yields of S3
Cumulative oil yield (mg/gTOC)
Pyrolysis temperature(℃)
(a) 2℃/h
(b) 20℃/h

Fig. 5

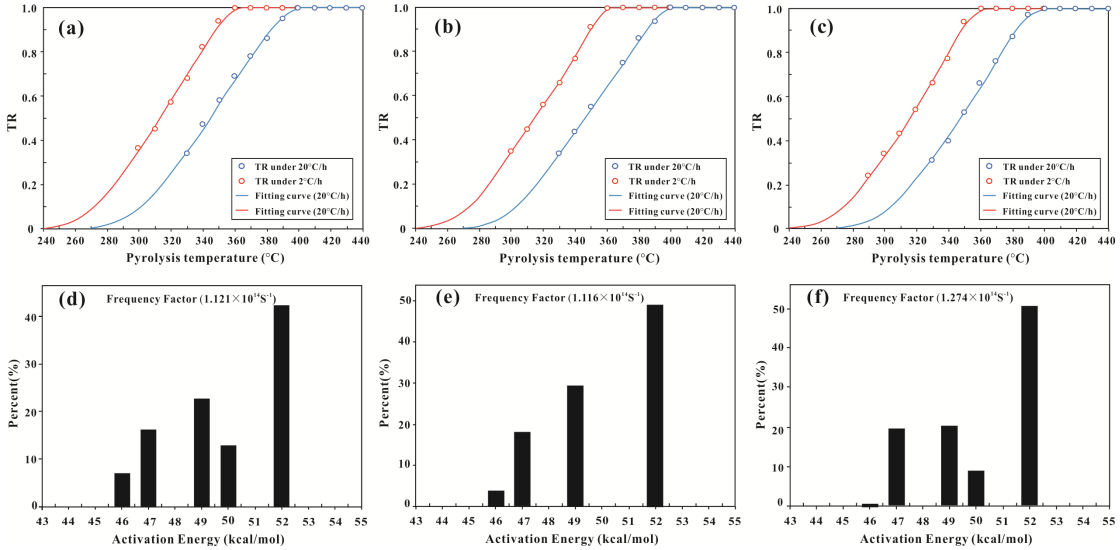
(a)
(b)
(c)
TR
Pyrolysis temperature (°C)
TR under 20°C/h
TR under 2°C/h
Fitting curve (20°C/h)
Fitting curve (20°C/h)

(d) Frequency Factor (1.121×10¹⁴S⁻¹)
(e) Frequency Factor (1.116×10¹⁴S⁻¹)
(f) Frequency Factor (1.274×10¹⁴S⁻¹)
Percent(%)
Activation Energy (kcal/mol)

Fig. 6

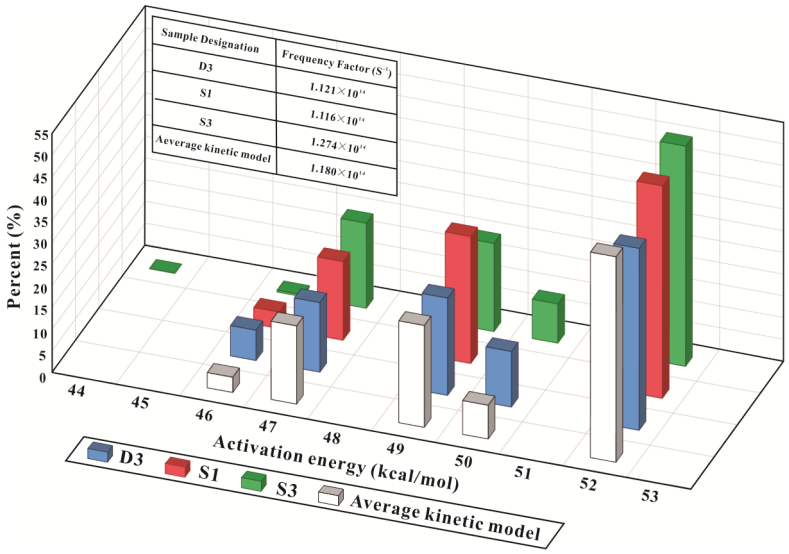
Sample Designation
Frequency Factor (S⁻¹)
D3
1.121×10¹⁴
S1
1.116×10¹⁴
S3
1.274×10¹⁴
Aeverage kinetic model
1.180×10¹⁴
Percent (%)
0
5
10
15
20
25
30
35
40
45
50
55
44
45
46
47
48
49
50
51
52
53
Activation energy (kcal/mol)
D3
S1
S3
Average kinetic model

Fig. 7

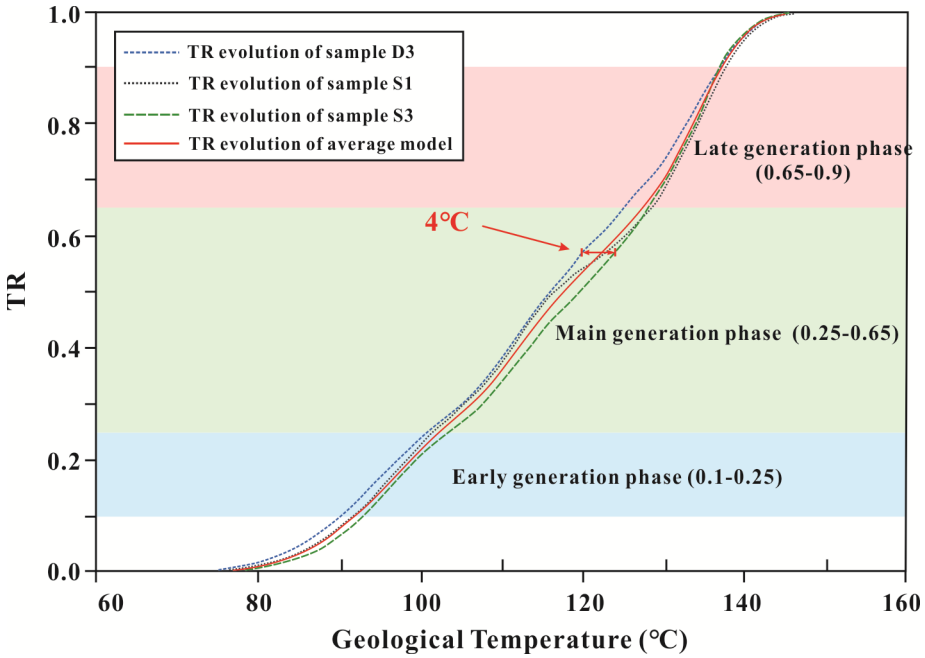
TR evolution of sample D3
TR evolution of sample S1
TR evolution of sample S3
TR evolution of average model
Late generation phase
(0.65-0.9)
4°C
Main generation phase (0.25-0.65)
Early generation phase (0.1-0.25)
TR
Geological Temperature (°C)
1.0
0.8
0.6
0.4
0.2
0.0
60
80
100
120
140
160

Fig. 8